# Impact of Gulf Stream Warm-Core Rings on Slope Water Intrusion into the Gulf of Maine

JIABI DU,[a] WEIFENG (GORDON) ZHANG,[a] AND YIZHEN LI[b]

[a] *Applied Ocean Physics and Engineering Department, Woods Hole Oceanographic Institution, Woods Hole, Massachusetts*
[b] *CSS Inc. at NOAA/National Centers for Coastal Ocean Science, Silver Spring, Maryland*

(Manuscript received 3 December 2021, in final form 7 April 2022)

ABSTRACT: Intruding slope water is a major source of nutrients to sustain the high biological productivity in the Gulf of Maine (GoM). Slope water intrusion into the GoM is affected by Gulf Stream warm-core rings (WCRs) impinging onto the nearby shelf edge. This study combines long-term mooring measurements, satellite remote sensing data, an idealized numerical ocean model, and a linear coastal-trapped wave (CTW) model to examine the impact of WCRs on slope water intrusion into the GoM through the Northeast Channel. Analysis of satellite sea surface height and temperature data shows that the slope sea region off the GoM is a hotspot of ring activities. A significant linear relationship is found between interannual variations of ring activities in the slope sea region off the GoM and bottom salinity at the Northeast Channel, suggesting the importance of WCRs in modulating variability of intruding slope water. Analysis of the mooring data reveals enhanced slope water intrusion through bottom-intensified along-channel flow following impingements of WCRs on the nearby shelf edge. Numerical simulations qualitatively reproduce the observed WCR impingement processes and associated episodic enhancement of slope water intrusion in the Northeast Channel. Diagnosis of the model result indicates that baroclinic CTWs excited by the ring–topography interaction are responsible for the episodically intensified subsurface along-channel inflow, which carries more slope water into the GoM. A WCR that impinges onto the shelf edge to the northeast of the Northeast Channel tends to generate stronger CTWs and cause stronger enhancement of the slope water intrusion into the GoM.

KEYWORDS: Continental shelf/slope; Channel flows; Mesoscale processes; In situ oceanic observations; Satellite observations; Numerical analysis/modeling

## 1. Introduction

Exchange processes between coastal and open oceans play an essential role in regulating the properties of coastal waters and dispersing coastal materials into the open ocean. One process that could greatly influence the cross-shelf water exchange is the impingement of western boundary current meanders or associated mesoscale eddies onto the edges of continental shelves (e.g., Malan et al. 2018, 2020). Mesoscale eddies shed from the Gulf Stream, so-called warm-core rings (WCRs), can induce strong cross-shelf water exchange when impinging onto the shelf edge in the Northwest Atlantic (e.g., Joyce et al. 1984; Churchill et al. 1986; Chaudhuri et al. 2009; Zhang and Gawarkiewicz 2015a, hereafter ZG15A; Bisagni et al. 2019) and substantially affect the heat, salt, and nutrient budget of the shelf seas (e.g., Churchill et al. 1986; Chen et al. 2014). The cross-shelf transport induced by ring–shelf interaction in the Northwest Atlantic can take on different forms:

1) Streamer offshore transport of the shelf water. Onshore propagation of the barotropic signal of a WCR can lead to offshore entrainment of the shelf water (Cherian and Brink 2016) and formation of a thermally distinctive submesoscale shelf-water filament, so-called *shelf water streamer*, in the slope sea (e.g., Garfield and Evans 1987; Joyce et al. 1992).
2) Subsurface export of shelf water. Observations from the Shelf Edge Exchange Processes (SEEP) arrays show near-bottom offshore transport of shelf water following the impingement of a WCR on the shelf edge (Churchill et al. 1986). This type of *subsurface* offshore transport of shelf water results from submesoscale frontal subduction on the intensifying ring–shelf water interface under the influence of an impinging WCR (Zhang and Partida 2018).
3) Direct intrusion of ring water onto the shelf. When an outward-extending limb of a WCR impinges onto the shelf edge, it extends along the shelf edge toward the downwave (southwest) while intruding slowly onto the outer shelf. This type of direct onshore intrusion of the ring water results from topographically induced vorticity variation of the ring water (ZG15A).

Note that the along-isobath directions in this work, namely, *upwave* or *downwave*, are in reference to the phase propagation of coastal-trapped waves (CTWs), which is a form of topographic vorticity wave associated with potential vorticity variation induced by the interaction between cross-isobath flow and sloping bottom (e.g., Clarke 1977; Huthnance 1978; Allen 1980; Brink 1991). CTWs in the north hemisphere propagate along isobath with the coast on the right.

Most studies of the dynamics of ring–shelf interaction consider the ring influence at a shelf with relatively simple topography, such as a straight shelf edge. Few studies consider the interaction between WCRs and irregular shelf and shelf-edge topography, e.g., shelf basin and shelf-break canyon. This study considers the interaction between Gulf Stream WCRs

*Corresponding author*: Weifeng (Gordon) Zhang, wzhang@whoi.edu

DOI: 10.1175/JPO-D-21-0288.1

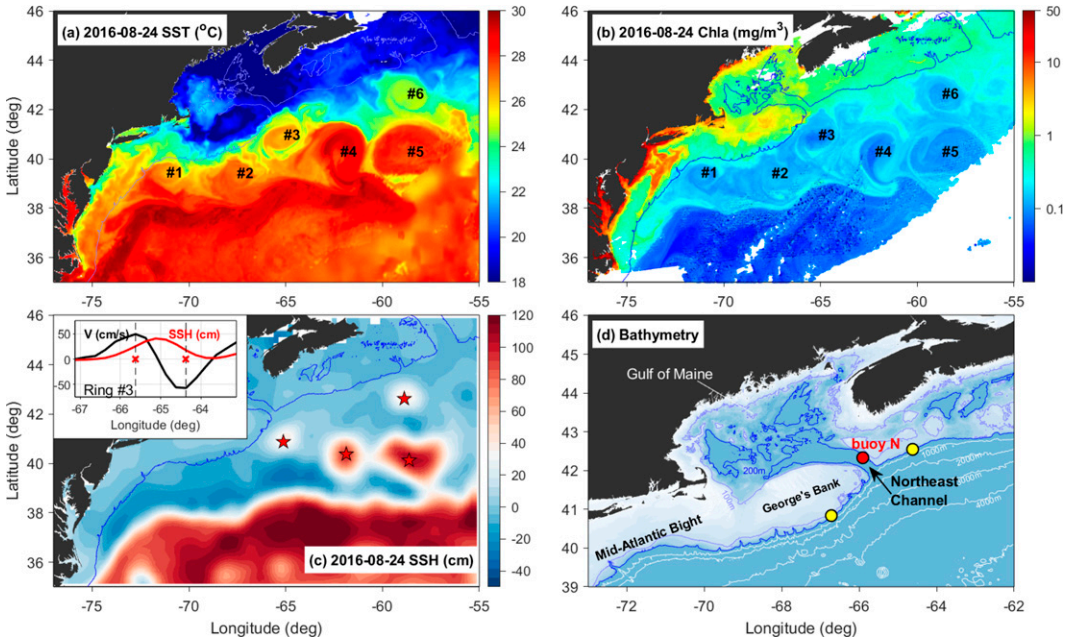


FIG. 1. Satellite images of (a) SST, (b) sea surface chlorophyll, and (c) SSH on 24 Aug 2016 highlighting six WCRs in the slope sea off the Mid-Atlantic Bight and GoM, four of which (3–6 as highlighted by the red stars) are detected automatically from the SSH data. (d) A zoom-in view of topographic features near the GoM, with dark blue lines denoting the 200-m isobath; light blue lines are the 100-m isobath; white lines are the 1000-, 2000-, 3000-, and 4000-m isobaths; the yellow dots indicate the upwave and downwave ends of the shelf edge considered in this study; and the red dot indicates the location of the mooring station (Buoy N) in the NEC. The inset in (c) shows a zonal section of the SSH (red line) and northward geostrophic velocity (black line) at 41°N (going through the center of ring 3), as well as the ring diameter (red crosses) determined from the velocity maxima.

and the topographically complex Gulf of Maine (GoM), which is a semienclosed shelf basin off the northeast coast of North America. While the GoM surface water is widely open with the Atlantic Ocean, its deeper part, below 100 m, is topographically confined and only connected with the Atlantic Ocean through the Northeast Channel (NEC), which is ~50 km wide, ~230 m deep, and northwest–southeast oriented (Fig. 1d). Given the complex topography, it is likely that the interaction of WCRs with the shelf edge off the GoM (including the southern edge of the Georges Bank) is more complex than the aforementioned ring–shelf interaction processes. One objective of this study is to characterize the ring–shelf interaction in this region of complex seafloor topography.

Cross-shelf exchange is important for the semienclosed GoM, one of the most important fishing grounds in the United States (Pershing et al. 2015). A major source of the nutrients to sustain the high biological productivity in the GoM is the subsurface water in the neighboring slope sea (hereafter referred to as *slope water*) intruding into the deep GoM (Townsend 1998; Townsend et al. 2010). The intruding slope water supplies ~30% of the nutrients needed for the primary biological production in the GoM (Schlitz and Cohen 1984). Changes in the slope sea conditions can cascade into the inner gulf via the nearly persistent slope water intrusion in the NEC (Smith et al. 2012) and then through the deep cyclonic circulations in the gulf (Bigelow 1927; Xue et al. 2000). Du et al. (2021) demonstrated a strong correlation between the bottom density and velocity in the NEC on the monthly time scale, with higher density corresponding to a stronger intrusion flow. This correspondence likely results from a strengthened inflow of the slope water in the channel leading to an increase of the water density there, as the subsurface slope water is generally denser than subsurface water in the GoM. Meanwhile, historical observations have shown that WCRs could dramatically change the temperature and salinity ($T$–$S$) property of the slope water near or in the NEC (Brooks 1987; Ryan et al. 2001; Smith et al. 2001; Du et al. 2021). However, the underlying mechanism associated with the ring-altered slope water intrusion into the gulf and whether the aforementioned relationship between bottom density and flow in the NEC is also true when a WCR impinges on to the nearby shelf edge remain unclear. Here, we analyze long-term mooring data and satellite remote sensing data to systematically examine the influence of WCRs on the slope water intrusion in the NEC over a variety of time scales and also to investigate the underlying dynamics.

## 2. Methods

### a. *Mooring data*

Historical measurements at a mooring station (Buoy N) in the NEC are analyzed to examine water $T$–$S$ property and along-channel velocity during WCR-impingement events. The mooring, sitting on the northeast side of the NEC, is part of the

University of Maine Ocean Observing System and Northeastern Regional Association of Coastal Ocean Observing Systems (NERACOOS). At Buoy N, six Seabird SE37 conductivity–temperature–depth (CTD) sensors were deployed at 1-, 20-, 50-, 100-, 150-, and 180-m depth, and an acoustic Doppler current profiler (ADCP) measures horizontal velocity in the depth range of 16–200 m at 8-m vertical resolution. The ADCP is mounted near the surface and looks downward. Hourly data from March 2004 to the present are available with minor gaps. More details of the buoy are given in Pettigrew et al. (2011). Time series of temperature, salinity, and velocity are low-pass filtered in this study with a cutoff frequency of 1/50 $h^{-1}$ to remove the tidal and diurnal fluctuations.

### b. Satellite data and ring detection

To quantitively examine ring activities in the slope sea, we implement a WCR autodetection algorithm based on the gridded global sea surface height (SSH) data in 1993–2018 (Mertz and Legeais 2020). In the algorithm, the SSH maxima are first identified based on the Okubo–Weiss parameter of a nondivergent horizontal flow,

$$W = 4\left[\left(\frac{\partial u}{\partial x}\right)^2 + \frac{\partial u}{\partial y}\frac{\partial v}{\partial x}\right], \tag{1}$$

that measures the relative importance of deformation and rotation. In (1), $u$ and $v$ are eastward and northward geostrophic velocity components, respectively, and they are computed from the satellite-measured SSH $h$, as $u = (-g/f)(\partial h/\partial y)$ and $v = (g/f)(\partial h/\partial x)$. Here, $g$ is the gravitational acceleration, and $f$ the Coriolis parameter. Following Isern-Fontanet et al. (2003) and Chelton et al. (2007), locations with $W < -2 \times 10^{-12}$ $s^{-2}$ are regarded as the center of an anticyclonic eddy. Because of the low spatial resolution (1/4°, ~20 km) of the SSH data, the autodetection scheme here identifies only WCRs with diameters close to or larger than 100 km, and neglects smaller rings or eddies that are unlikely to cause substantial cross-shelf exchange. For instance, on 24 August 2016, there were a total of 6 WCRs visually noticeable from satellite images of sea surface temperature (SST) and sea surface chlorophyll in the region between 55° and 75°W, but only the four larger ones are detected by the algorithm (Fig. 1).

### c. Idealized numerical primitive equation model

An idealized model, based on the Regional Ocean Modeling System (ROMS; Shchepetkin and McWilliams 2005), is used in this study to uncover the underlying mechanisms of WCRs affecting the slope water intrusion. Following ZG15A, the model solves nonlinear momentum and density equations in a rectangle domain with a continental shelf and slope oriented in the east–west ($x$) direction and along-shelf periodic boundaries. The coast is at the northern boundary, and the southern boundary is located in the deep ocean. The inshore 541 km of the model domain covering the gulf (see below), continental shelf, slope, and part of the deep ocean is the study region with no explicit horizontal viscosity and diffusivity. South of the study region is a sponge layer where horizontal viscosity and diffusivity increase linearly southward, reaching 100 $m^2$ $s^{-1}$ at the southern boundary. The grid size is 500 m in the central study region and increases gradually toward the south, east, and west boundaries. A general length scale vertical turbulence closure $k$–$kl$ scheme (Warner et al. 2005) and quadratic bottom drag with drag coefficient of 0.003 are used. There is no surface forcing. Several aspects of the model configuration are modified from ZG15A:

1) The model domain is substantially extended in the east–west direction to 7770 km to delay the return of westward propagating barotropic shelf/slope waves to the middle of the domain after they pass through the east–west periodic boundary. These waves have elevated signals near the shelf edge and are likely higher-mode barotropic topographic vorticity waves excited by WCRs impinging onto the shelf edge. Once returning to the generation site, they can affect the exchange flow in the channel. This impact of the barotropic shelf/slope waves is beyond the scope of this study. The extension of the model domain delays the return of the waves to after 50 days, and the analysis here focuses on the first 50 days of the simulations.
2) An idealized gulf with a near-rectangular shape is added to the shelf topography (Fig. 2a). Below 100 m, the gulf is connected to the slope sea through a 50-km-wide channel. The gulf topography $h_{\text{gulf}}$ is added to the background bathymetry in ZG15A as

$$a_g = 1 + \frac{(a_0 - 1)}{2}\left[1 + \tanh\left(\frac{y - y_e}{l_t}\right)\right], \tag{2}$$

$$f_a = \frac{1}{2}\left[\tanh\left(\frac{x - x_o - w_o a_g}{a_g^{1/2} l_{\text{sa}}}\right) - \tanh\left(\frac{x - x_o + w_o a_g}{a_g^{1/2} l_{\text{sa}}}\right)\right], \tag{3}$$

$$f_c = \frac{1}{2}\left[\tanh\left(\frac{y - y_o - w_g}{l_{\text{sc}}}\right) - \tanh\left(\frac{y - y_o + w_g}{l_{\text{sc}}}\right)\right], \tag{4}$$

$$h_{\text{gulf}} = f_a f_c h_c. \tag{5}$$

Here, $h_c = 250$ m is the gulf depth scale, $(x_o, y_o)$ is the coordinate of the gulf center, $w_o = 15$ km is the channel width scale, $l_{\text{sa}} = 5$ km and $l_{\text{sc}} = 20$ km are the along- and across-shelf length scales of the topographic transition from the shelf to the gulf, respectively, and $w_g = 110$ km is the cross-shelf length of the gulf, $a_0 = 10$ is the ratio of gulf width to channel width.
3) A beta plane (instead of the $f$ plane in ZG15A) is applied with $f$ increasing toward the northeast direction in the central part of the model domain (3500 km to the west and east of the channel) to resemble the change of $f$ in the real ocean relative to the orientation of the GoM. This modification allows WCRs initially placed in the deep ocean to migrate northwestward (in the model coordinate) toward the shelf edge under the influence of nonlinear Rossby wave propagation (Early et al. 2011). Note that, outside of the central domain, $f$ changes in the

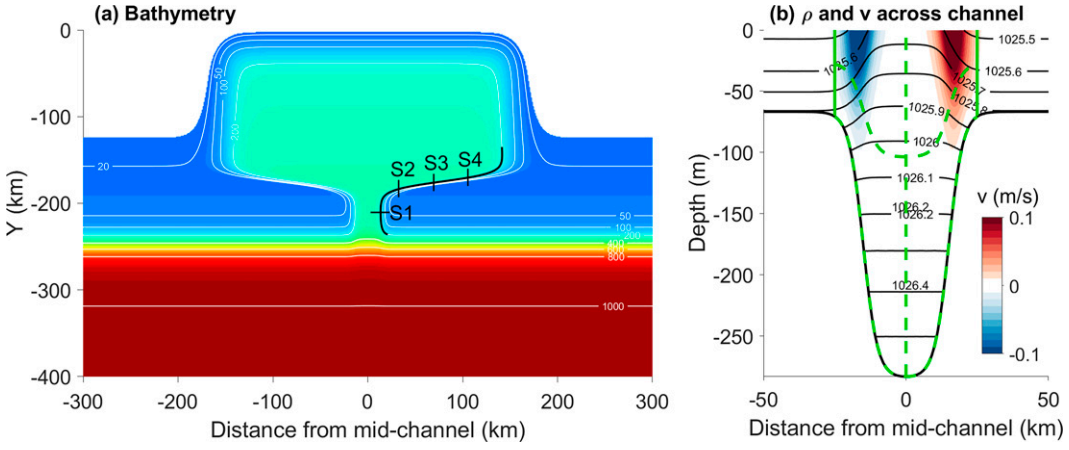


FIG. 2. (a) Idealized seafloor topography of the model; (b) along-shelf (cross-channel) section of the initial along-channel velocity (color) and potential density (black contours) at $y = 200$ km. The white lines in (a) are isobath contours; the bended black line in (a) shows the section of the 200-m isobath where the along-isobath propagation of coastal-trapped waves is examined (Fig. 13); and the short black lines in (a) denote the cross-isobath sections, S1–S4, where along-isobath velocity is plotted in Figs. 14 and 16. The green solid and dashed lines in (b) show the channel cross-sectional area and the four quadrants used for computing the mean along-channel velocity (see text), respectively.

opposite way, which gives the same value of $f$ on the eastern and western boundaries, as required by the periodic boundary condition.

4) A cross-isobath density front and frontal jet imposed in the model initial condition follow the bended 150-m isobath into the gulf (Fig. 2a), which differs from the straight shelf-break front and jet in ZG15A. The frontal jet centers at the 150-m isobath and forms an inflow (outflow) at the eastern (western) side of the channel (Fig. 2b). The inflow is one key feature of the NEC (Smith et al. 2012; Fratantoni and Pickart 2007). The shelf-break frontal jet is introduced by adding an additional density anomaly to the background density profile, following Zhang and Gawarkiewicz (2015b).
5) Cyclogeostrophic balance (instead of geostrophic balance as in ZG15A), which considers the centrifugal acceleration (Penven et al. 2014), is used here to compute the initial ring velocity from the prescribed ring water density anomaly

$$\Delta\rho_r(x,y,z) = \frac{\Delta\rho_0}{2}\left[1 - \tanh\left(\frac{r - r_c}{r_b}\right)\right]\exp\left(\frac{-z^2}{h_r^2}\right). \quad (6)$$

Following Knox and Ohmann (2006), cyclogeostrophically balanced azimuthal velocity,

$$V = \frac{2V_g}{1 + \sqrt{1 + 4V_g/(fr)}} \quad (7)$$

and the associated sea level tilt in the ring area (within $r_c + 2r_b$ from the ring center) are added to the model initial conditions. Here, $V_g$ is the geostrophic velocity, calculated from the thermal wind balance, $r$ is the distance from the ring center.

To quantify the water exchange through the channel, we employ four Eulerian passive tracers in the model to represent concentrations of gulf, shelf, slope, and ring waters. Initial values of the passive tracer are 1 in the three-dimensional volume of the corresponding water masses and 0 elsewhere. Time series of fluxes of the passive tracers in the channel are calculated from the modeled velocity and passive tracer fields (see below).

### d. Linear coastal-trapped wave model

A two-dimensional (vertical and cross-shelf) linear model of inviscid CTWs (e.g., Brink 1990, 2006) is used in this study to simulate baroclinic CTWs along a straight coast. Details of the model are described in Zhang and Lentz (2017). The model uses an idealized cross-shelf bathymetry to represent the northeastern slope of the NEC (see below). It employs a free-slip bottom boundary condition, a free surface condition, a closed wall condition on the coast, and a zero-gradient condition on the offshore boundary. The cross section is discretized into 200 and 57 uniform grid intervals in the cross-shelf and vertical directions, respectively. With a constant $f$, a uniform stratification and no background flow, the model numerically solves a pressure-based vorticity equation to look for CTW solutions with a wave form in both time and the along-isobath direction, as well as a modal structure in the cross-shelf and vertical directions. The results are the CTW dispersion curves for different cross-shelf modes, as well as cross-shelf and vertical distributions of pressure and velocity associated with each mode.

## 3. Results

### a. WCR activities

Analysis of the SSH data in 1993–2018 shows that the slope sea region to the immediate southeast of the GoM has more intense ring activities than any other region of the slope sea in the northwest Atlantic. Within the 26 years, some of the 1/4° × 1/4° grids within the slope sea region off the GoM had

over 50 rings passing through (Fig. 3a). Meanwhile, the same region has the highest ring occupancy with up to 35% of the time being within a WCR (Fig. 3b). Here, a location is considered within a WCR if its distance from the ring center is less than $2r_c$, with $r_c$ being the radial distance between the maximum geostrophic azimuthal velocity and the ring center (see the inset in Fig. 1c).

To quantify the impact of WCRs on the physical conditions in the GoM, we first count WCRs in the vicinity of the NEC using the autodetection algorithm. It shows that the slope sea region within 1° longitude range around the NEC (i.e., 66.7°–64.7°W) and 50 km off the shelf edge is occupied by at least one ring for 53% of the time. As the rings have a diameter scale of 100–150 km, rings within 50-km proximity of the shelf edge can likely cause substantial exchange across the shelf edge (e.g., ZG15A; Zhang and Partida 2018). Meanwhile, monthly climatology of the ring presence near the GoM shows a seasonality with two peaks, a major one in August and a secondary one in December (Fig. 4c). The peak in August is consistent with the fact that more WCRs are formed from the Gulf Stream during May–July (Gangopadhyay et al. 2019), as it usually takes 1–2 months for the rings to propagate westward before reaching the shelf edge.

On the interannual time scale, our analysis shows a significant correlation between WCR activities and measured bottom salinity (deeper than 100 m) in the NEC (Fig. 4e). Here, WCR activities are represented with the number of days ($d_{\text{ring}}$) in each calendar year when there is a WCR within 50 km proximity of the shelf edge off the GoM. Within the 14 years (2004–17) when both the SSH and mooring salinity datasets are available (Figs. 4b,d), $d_{\text{ring}}$ varies from 50 to 300 days. The significant relationship between $d_{\text{ring}}$ and the bottom salinity in the NEC suggests that, on the interannual time scale, ring activities in the slope sea region off the GoM influence offshore water intrusion in the NEC. This influence of the WCRs can be carried out through two potential pathways: (i) WCRs modify properties of the source slope water in the slope sea and *indirectly* affect the intrusion in the NEC, and (ii) WCRs *directly* affect the slope water intrusion in the NEC dynamically. The former is presumably carried out through mixing, while the latter through advection. Because flows associated with WCRs are generally strong, Péclet number, the ratio of advective to diffusive transport, i.e., $\text{Pe} = LU/\nu_h$, of the ring influence is likely large. Here, $L$ is the horizontal length scale, $U$ is the velocity scale, and $\nu_h$ is the horizontal diffusivity. The time scale of the indirect influence is likely much longer than the episodic event time scale that the direct influence occurs over. Because this study focuses on the dynamics of the ring influence, we will examine the *direct* pathway in the following sections. The longer-term *indirect* pathway will be discussed in section 4b.

Our analysis also shows that more WCRs are present in the slope sea region to the southwest of the NEC, compared to the slope sea region to the northeast of the NEC (Fig. 4b). As will be demonstrated in section 4, a WCR impinging on the shelf edge to the *northeast* of the NEC tends to induce more offshore water intrusion in the NEC than a WCR impinging onto the shelf edge to the *southwest* of the NEC. Therefore, although WCRs enhance the offshore water intrusion into the GoM, their northeast–southwest asymmetrical distribution with respect to the NEC diminishes the effectiveness of the enhancement.

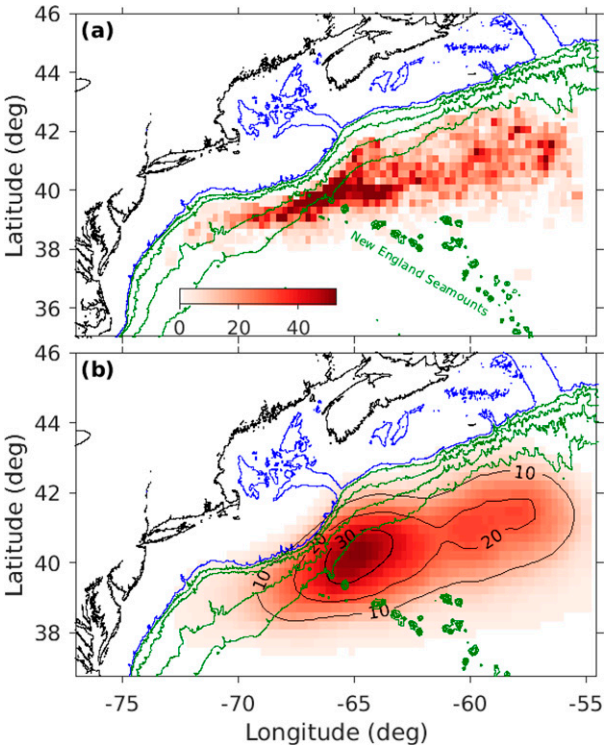


FIG. 3. Spatial variation of WCR activities computed from SSH data in 1993–2018: (a) the number of rings whose centers have passed through each of the 1/4° × 1/4° grid; (b) percentage of time (%) of each 1/4° × 1/4° grid being within a WCR. The blue lines represent 200 m isobath contours; and the green lines represent 1000-, 2000-, 3000-, and 4000-m isobath contours.

### b. *Impact of WCRs on the flow in the NEC*

We now choose three representative WCRs impinging onto the shelf edge off the GoM to examine the process of ring influencing the flow in the NEC on the event time scale. The selected rings all stayed in the slope sea region off the GoM for at least one month. They impinged onto different locations of the shelf edge relative to the NEC and had different impacts on slope water intrusion.

In June–August 2017, a WCR (hereafter referred to as R17) impinged onto the shelf edge to the northeast of the NEC and induced significant intrusion of slope and ring waters in the NEC. In situ measurements at Buoy N show episodic *subsurface* intrusion of warm and saline water in the NEC. In particular, the bottom-layer (below 100 m) temperature and salinity increased dramatically on 24 June and 4 July in concert with positive inflow at the depth of 100–150 m, as highlighted in Figs. 5g and 5h. Before the ring impingement on 19 June, near-bottom salinity in the NEC remained below 34.6 for several months. During the two episodic intrusion events that are 10 days apart, the bottom-layer salinity in the

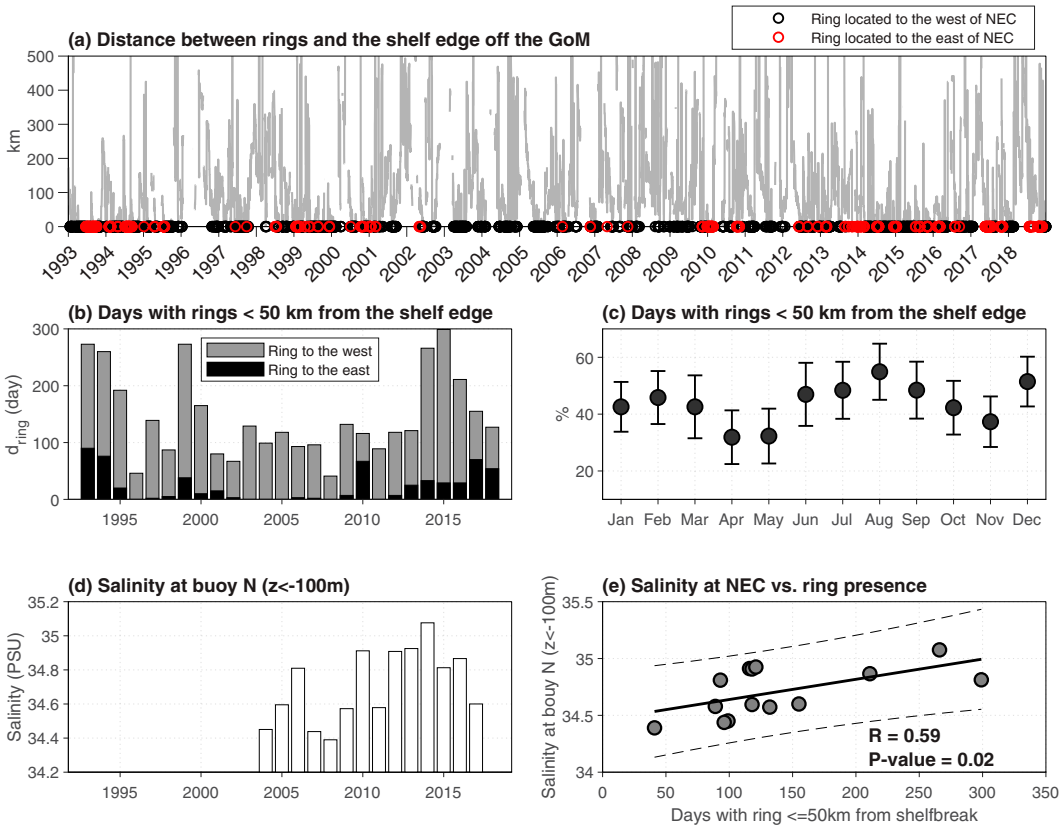


FIG. 4. Presence of WCRs in the slope sea region off the GoM and its relationship with the bottom salinity in the NEC. (a) Time series of the minimum distance between rings and the shelf edge (200-m isobath) off the GoM, with black and red circles indicating the along-shelf position of the ring centers relative to the NEC. (b) Interannual variations of the number of ring-occupying days in a year (defined as the days when there is at least one ring within 50 km proximity of the shelf edge off the GoM). Black and gray bars indicate the times of the rings located to the east and west of the NEC, respectively. (c) Climatology of the percentage of time in each month of at least one ring being present within 50-km proximity of the shelf edge off the GoM with error bars representing one standard deviation. (d) Annual mean salinity of the bottom water measured at Buoy N in the NEC. (e) Relationship between annual mean bottom salinity in the NEC and the number of ring-occupying days in a year, with the solid and dash lines denoting a least-squared fit and its 95% confidence, respectively.

NEC increased from 34.6 to 35.5 and from 34.5 to 35.7, respectively. As salinity values of >35 and >35.5 are recognized as the signature of slope water and Gulf Stream (and WCR) water, respectively (Houghton and Fairbanks 2001), the in situ measurements indicate that, coinciding with the WCR impingement, warm slope and ring waters intrude into the NEC. Note that because in situ data after 16 July are missing, it is unclear whether more episodic intrusion occurred afterward. Meanwhile, the near-bottom density in the period of 19 June–16 July vary over the same event time scale, and its variation appears to lag the variation of inflow velocity by 2–5 days (Figs. 5g,h). The lag correlation between daily-averaged near-bottom density and velocity over the period reaches the maximum of 0.83 with a $P$ value of $6.4 \times 10^{-6}$, when the density lags velocity by 2 days. The facts that variations of near-bottom density and velocity occur over the same event time scale and velocity variation leads density variation suggest that the episodic intrusion of slope and ring waters into the channel is likely driven by the ring-induced enhancement of the subsurface inflow, i.e., the aforementioned *direct* impact of the WCR impingement.

In August–October 2016, another WCR (hereafter referred to as R16) impinged onto the southeast edge of the Georges Bank (to the southwest of the NEC) and also induce significant slope water intrusion in the NEC. SST images show that, after developing from an elongated Gulf Stream meander in the beginning of August, R16 migrated westward and stayed in the slope sea region off the GoM till October with no indication of *surface* intrusion of the warm water into the NEC (Figs. 6a–f). After R16 impinged onto the southeast edge of the Georges Bank in mid-August (Fig. 6c), in situ measurements at Buoy N show bottom-layer temperature and salinity increased episodically in concert with positive near-bottom inflow (see highlights in Figs. 6g,h). In particular, strengthened slope water intrusion occurred on 10 August, as indicated by a dramatically enhanced subsurface inflow velocity with the

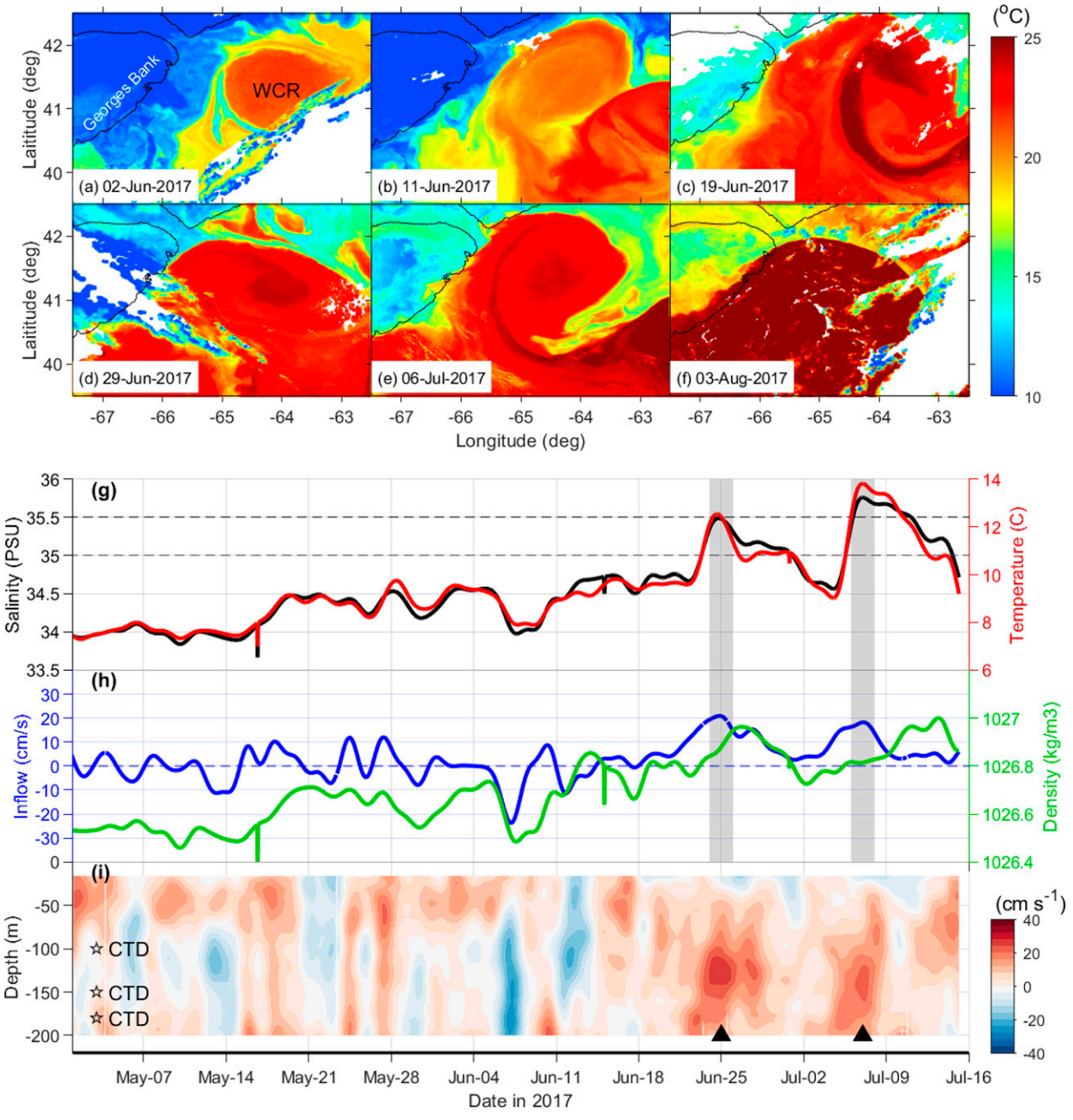


FIG. 5. (a)–(f) Satellite SST images in June–August 2017 showing the evolution of R17 impinging on the shelf edge northeast of the NEC. Time series of measured bottom-layer (g) salinity (black line) and temperature (red line) and (h) along-channel velocity (blue line) and density (green line), as well as (i) vertical profile of along-channel velocity at Buoy N in the NEC. Gray shading in (g) and (h) highlights periods of enhanced slope water intrusion; stars in (i) indicate depths of the near-bottom CTDs, and the thick black line in (i) indicates the seafloor depth. Note that tidal signals have been removed in the time series data in (g)–(i), and that the time series in (g)–(i) end on 16 July owing to an extensive period of missing data after that.

maximum speed $>$ 40 cm $s^{-1}$ at 150-m depth (Fig. 6i). The near-bottom intensified inflow velocity differs distinctively from other periods when the maximum inflow velocity was in the upper water column (50–100 m). The intensified near-bottom inflow on 10 August coincided with rapid increases of bottom-layer temperature from 9° to 12°C and salinity from 34.7 to 35.4. At least two more intrusion episodes occurred after that, on 21 and 30 August, respectively, with similar or greater bottom-layer temperature and salinity increases. The changes of salinity clearly indicate episodic intrusion of slope and ring waters into the NEC. Interestingly, similar to those in 2017, the intrusion episodes in August 2016 are also

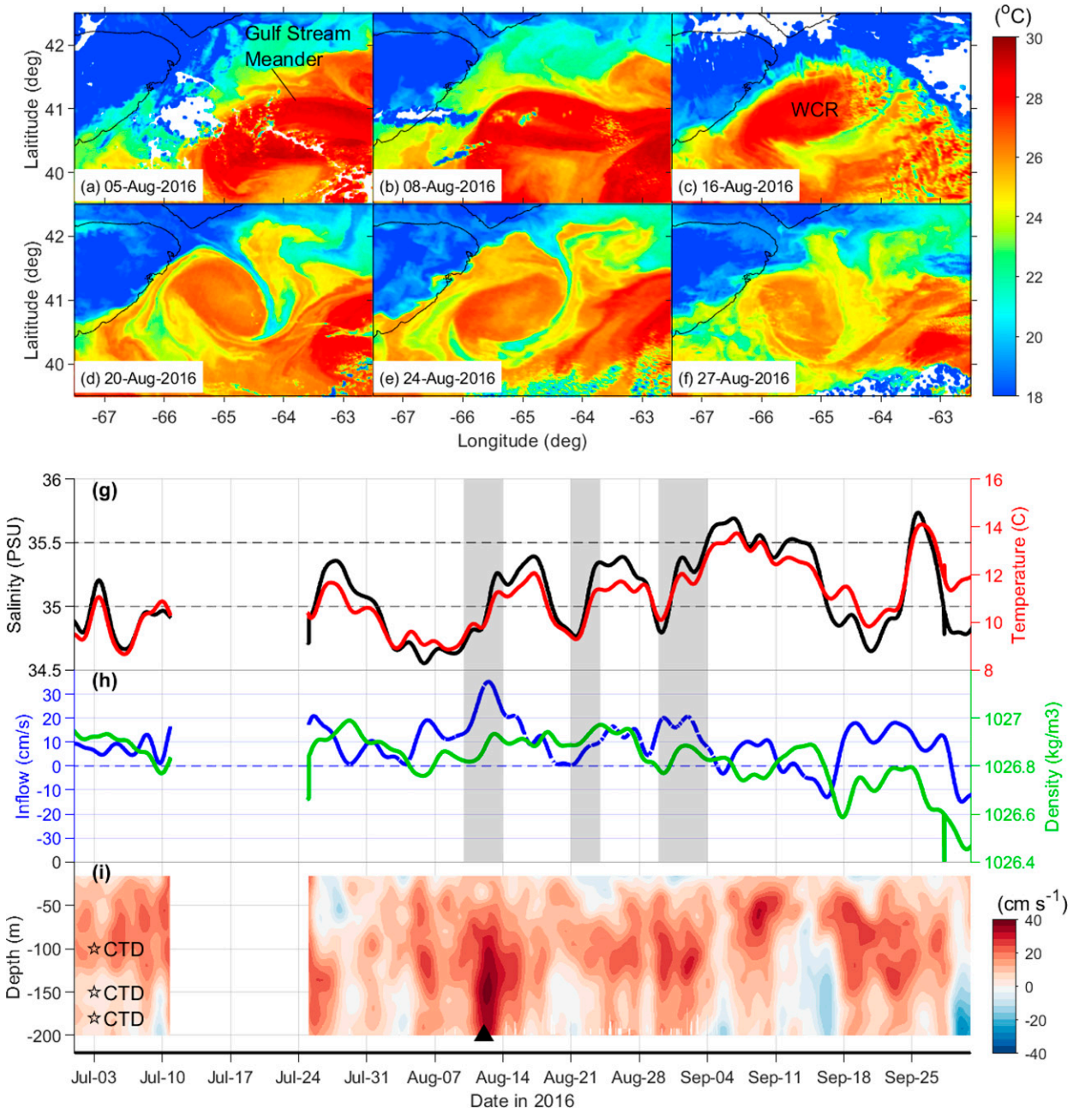


FIG. 6. (a)–(f) Satellite SST images in August 2016 showing the evolution of R16 impinging on the southeast edge of the Georges Bank (to the southwest of the NEC). Time series of measured bottom-layer (g) salinity (black line), temperature (red line) and (h) along-channel velocity (blue line) and density (green line), as well as (i) vertical profile of along-channel velocity at the mooring station in the NEC. Gray shading in (g) and (h) highlights periods of enhanced slope water intrusion; stars in (i) indicate depths of the near-bottom CTDs, and the thick black line in (i) indicates the seafloor depth. Note that tidal signals have been removed in the time series data in (g)–(i).

separated by ~10 days. This time interval is related to the dynamics of the slope/ring water intrusion into the NEC, which will be examined in section 4a. Meanwhile, a lag-correlation analysis of the data in August–September 2016 shows that the increases of along-channel inflow lead the increases of bottom-layer density by ~1.5 days (Fig. 6h), also suggesting the enhanced subsurface inflow causes the episodic slope/ring water intrusion into the NEC. Note that the buoy measurements show a sustained inflow over 17–27 September and a dramatic increase of temperature and salinity on 24–25 September. This event of slope/ring water intrusion does not appear to be directly related to the WCR that had migrated to the southwest at the time and is likely caused by other processes in the ocean.

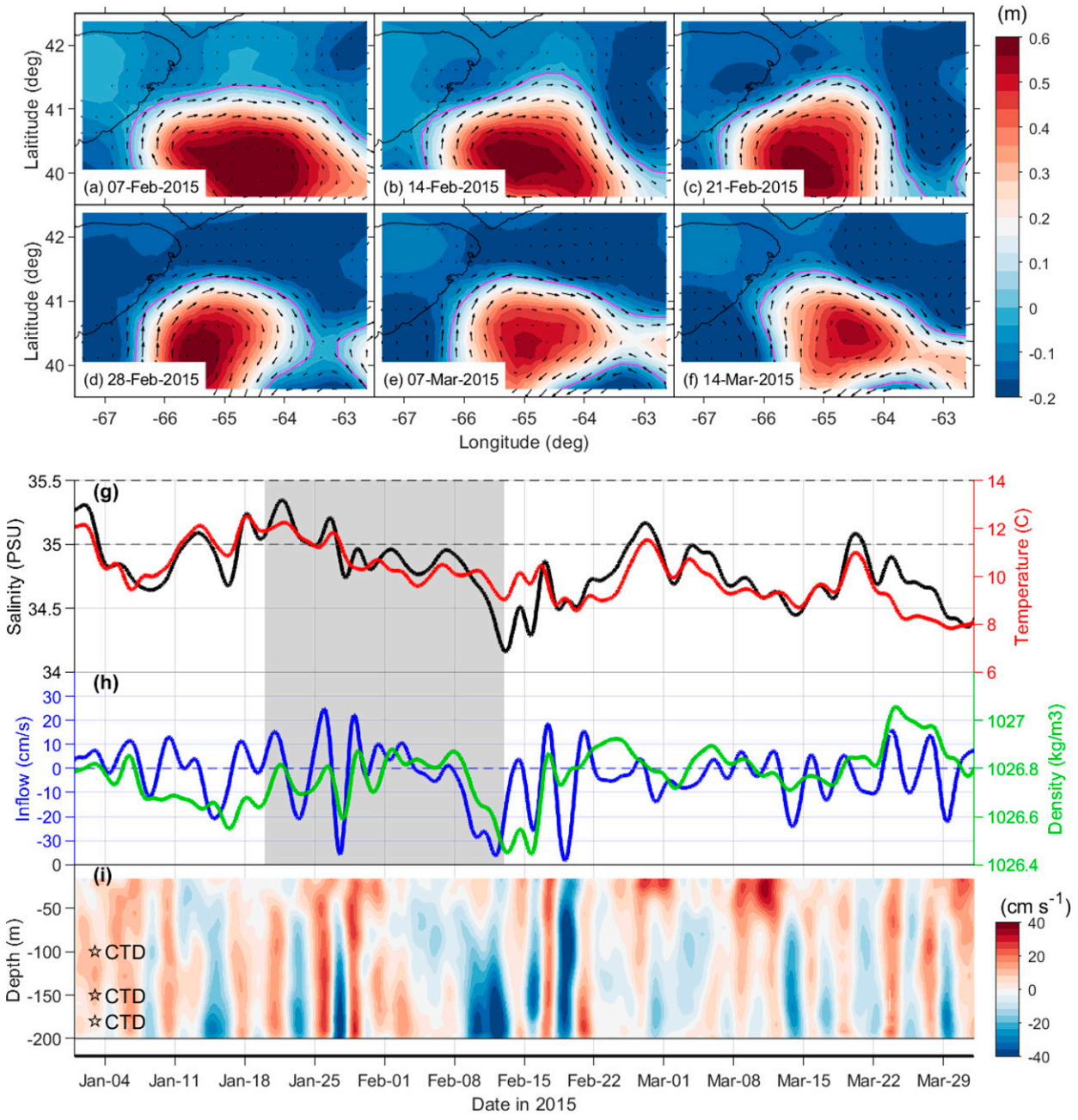


FIG. 7. (a)–(f) Satellite-measured SSH (color) and derived surface geostrophic current (arrows) in February–March 2015 showing the evolution of R15 impinging on the southeast edge of the Georges Bank. Time series of measured bottom-layer (g) salinity (black line) and temperature (red line) and (h) along-channel velocity (blue line) and density (green line), as well as (i) vertical profile of along-channel velocity at the mooring station in the NEC. Note that tidal signals have been removed in the time series data in (g)–(i). In (a)–(f), magenta lines are the SSH contour of 0 m, which represent the edge of the ring; only geostrophic velocity with speed $> 0.1$ m s$^{-1}$ is shown. Gray shading in (g) and (h) highlights the period of decreasing bottom-layer temperature and salinity; stars in (i) indicate depths of the near-bottom CTDs, and the thick black line in (i) indicates the seafloor depth.

WCR impingement onto the shelf edge off the GoM does not always lead to clear enhancement of the warm slope/ring water intrusion in the NEC. For instance, in February–March 2015, a WCR (hereafter referred to as R15) stayed in the slope sea region off the GoM for over a month with no clear indication of intensified warm water intrusion in the NEC (Fig. 7). Because of intensive cloud cover over the period, no clear SST satellite images are available. Instead, SSH data are used to illustrate the ring evolution. R15 impinged onto the south edge of the Georges Bank (farther west from the NEC

than R16) in the beginning of February. Meanwhile, the in situ measurements show decreasing bottom-layer temperature and salinity in the NEC over the period from 20 January to 13 February (as highlighted in Figs. 7g,h). After that, the bottom-layer temperature and salinity increased gradually. But the maximum salinity only reaches 35.2 on 28 February, and there was no clear signal of episodically enhanced intrusion of warm and saline slope water in the NEC. The vertical profile of along-channel velocity does not show any strong subsurface inflow event, either (Fig. 7h), and temporal variation of the along-channel velocity was mostly barotropic, likely responding to changing surface winds (Ramp et al. 1985; Wright et al. 1986).

The different responses of the flow in the NEC during these WCR impingement events suggest that the influence of WCRs on the slope water intrusion is complex. Presumably, it varies with the slope water conditions, ring characteristics (e.g., radius, density anomaly and instability), the relative locations of the ring and the NEC, as well as external forcing, such as winds. Given all these factors, it is difficult to explain the dynamics of specific responses of the channel flow to the impingement of a particular WCR. Nevertheless, the similarity between the channel flow responses to R16 and R17 intrigues us to examine the fundamental dynamics of the ring impingement enhancing the intrusion of the slope/ring water into the GoM through the NEC. Moreover, the near-bottom intensification of the intrusion flow and its periodicity under the influence of R16 and R17 resemble characteristics of baroclinic CTWs of higher modes (e.g., Brink 1991, 2006). We thus hypothesize that the pulse-like enhancement of slope/ring water intrusion during a WCR impingement is induced by CTWs that are excited by the ring–topography interaction. To verify that, we conduct a series of idealized ROMS simulations to focus on the impact of WCRs in the channel while neglecting other forcing factors that could also affect the channel flow in the real ocean. Motivated by the ring impingement events above, we will consider the influence of impingement site by placing WCRs at different locations relative to the channel.

### c. *ROMS modeling of the ring–channel interaction*

Four ROMS simulations, namely, Base, EXP1, EXP2, and EXP3 runs are conducted. The Base run has the aforementioned idealized shelf and gulf topography, but no WCR. It serves as a reference to examine the influence of WCRs on the exchange flow in the channel. In EXP1, EXP2, and EXP3, WCRs are added to the deep ocean to the south, southeast, and southwest of the channel, respectively. Evolution of the WCR and its interaction with the shelf edge and channel in EXP1 are shown in Fig. 8. The idealized model qualitatively reproduces key features in the SST images, including westward migration of the WCR, distortion and deformation of the ring, and formation of a shelf-water streamer and an elongated ring limb extending downwave along the shelf edge. These features are also qualitatively reproduced in EXP2 and EXP3 (not shown).

Comparisons among the simulations suggest that WCRs generally enhance the intrusion of offshore water in the channel, but the enhanced intrusion flux varies among the simulations. In the Base run, vertically integrated total volume flux in the first 20 days is positive (influx; toward the gulf) and negative (outflux; toward the ocean) on the eastern and western parts of the channel, respectively, which results from the along-isobath shelf break frontal jet extending into the gulf through the channel (Fig. 9e). After day 20, an inflow appears on the western part of the channel, while the outflow migrates to the middle of the channel. This results from an anticyclonic eddy forming from instability of the horizontally sheared frontal flow moving into the channel. Meanwhile, the influx of the slope water passive tracer in the channel is weak and changes relatively little over the 50-day simulation period (Fig. 9i).

The model qualitatively reproduces the observed episodic enhancement of slope water intrusion in the channel during ring impingement periods. When an idealized ring impinges onto the mouth of the channel (EXP1), there are dramatic increases of the influxes of both total volume and the slope water on the eastern part of the channel starting from day 20 (Figs. 9f,j). Strengthening of the influxes on the eastern part of the channel occurs twice with a 10-day interval (on days 20 and 30), and the increased influx of total volume is compensated by a stronger outflux on the western part of the channel. Overall, the slope water influx in the channel is greatly enhanced in EXP1, compared to the Base run (Figs. 9i,j).

When the ring impinges onto the shelf edge to the east of the channel (EXP2), influxes of both total volume and slope water on the eastern part of the channel are strengthened on days 27 and 37 (Figs. 9g,k). The 10-day interval between the two influx pulses is consistent with that in EXP1 and also observations following the impingement of R17 (Fig. 5) and R16 (Fig. 6). Meanwhile, starting on day 24, there is a strong influx of the slope water in the middle of the channel lasting for ~3 days. This short-lived influx event results from an elongated limb of the ring impinging over the mouth of the channel pushing slope water inward across the entire channel.

In EXP3 where the idealized ring impinges onto the shelf edge to the far west of the channel, the volume influx and the slope water intrusion in the channel are slightly stronger than those in the Base run, but much weaker than in EXP1 and EXP2 (Figs. 9h,l). This weak impact of the ring is consistent with observations showing no clear disturbance to the flow in the NEC after R15 impinging onto the southern edge of the Georges Bank (to the west of the NEC) (Fig. 7).

To further illustrate the ring impact on the channel flow, we calculated time-averaged, vertically integrated along-channel fluxes of slope, ring, and gulf waters based on the simulated passive tracers (Fig. 10). The fluxes are averaged over a 20-day period, starting from day 20 when the ring impact becomes visible in the channel. The along-channel flux of slope and ring waters together averaged over the 20 days and across the entire channel is $\sim 53 \times 10^3$ m$^3$ s$^{-1}$ (toward the gulf) in both EXP1 and EXP2. In contrast, the averaged net along-channel flux of slope and ring water together is only $7 \times 10^3$ in EXP3. As the ring evolution is qualitatively

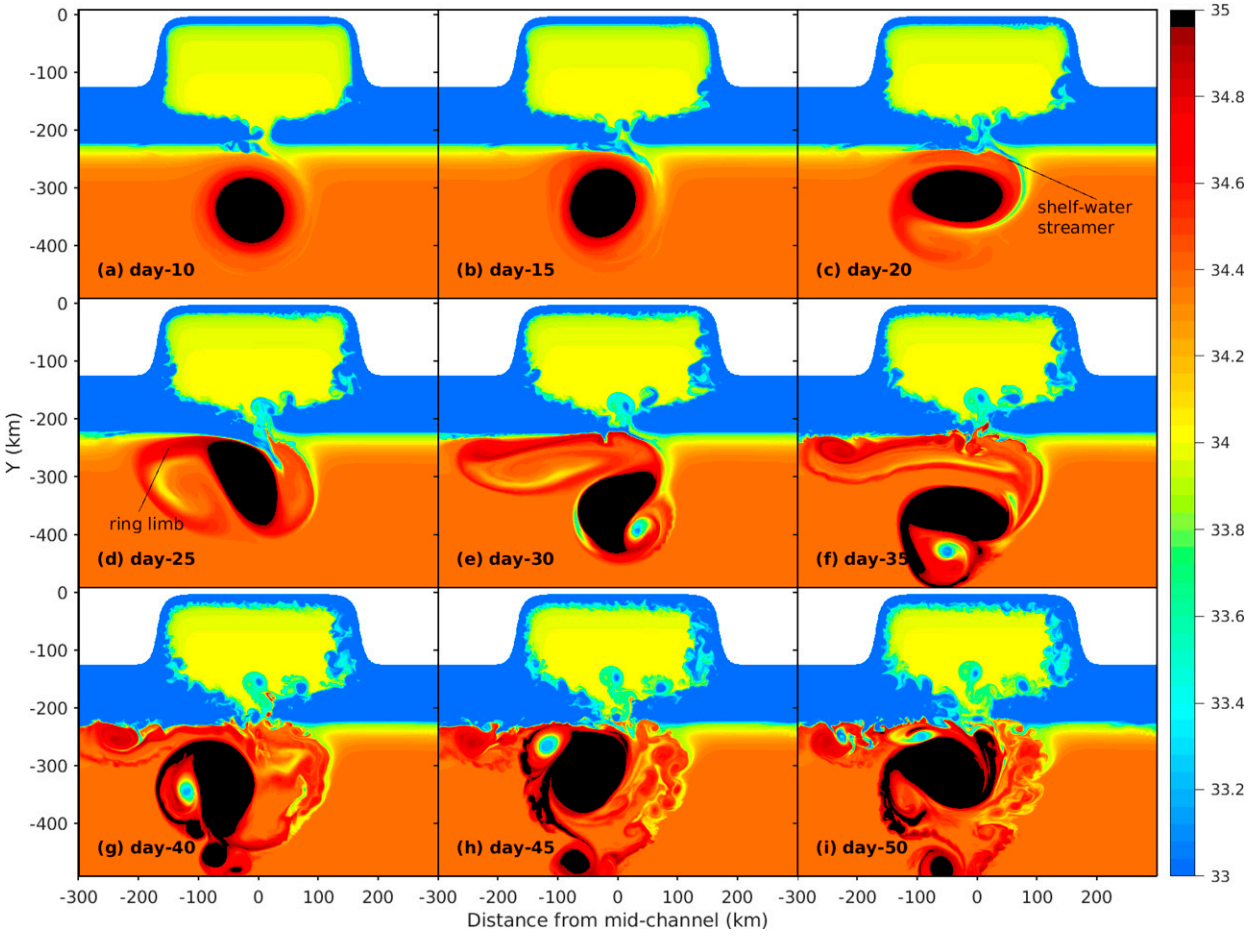


FIG. 8. Snapshots of modeled surface salinity from EXP1, showing the evolution of an idealized WCR initialized off the shelf edge.

similar in the simulations, especially, in EXP1 and EXP3 (Figs. 9b,d), differences in ROMS-simulated enhancement of the along-channel influx of slope and ring waters suggest that the position of the impinging ring relative to the channel plays a key role in regulating the channel flow. The underlying dynamics is explored in the following section.

## 4. Discussion

### *a. Mechanism of the intermittent offshore water intrusion*

This section is to examine the dynamics of the offshore (ring and slope) water intrusion in the channel. We focus on episodic enhancement of the intrusion associated with the ring impingement, rather than the long-term mean intrusion in the channel that have been documented in the literature. We first divide the channel cross section into four quadrants (Fig. 2b) and examine the time evolution of the mean along-channel velocity in each of the quadrants in EXP1. The along-channel velocity averaged over every quadrant has two major peaks, one on days 20–22 and the other on days 29–31 (Fig. 11a). The quadrant-averaged velocity time series normalized by the corresponding temporal mean velocity in the first 10 days show that velocities in the bottom quadrants are enhanced much more substantially than those in the surface quadrants (Fig. 11b). For instance, in the eastern half of the channel, the bottom-layer inflow is increased by 800% during the first peak, while the surface-layer velocity is enhanced by only 80%. During the second peak, the surface-layer velocity in the eastern half of the channel reaches its initial level of ~4 cm $s^{-1}$, while the bottom-layer velocity increases to ~500% of its initial level. These point to an interesting feature: the episodically enhanced inflow velocity in the eastern part of the channel is bottom intensified (see below).

We now examine the vertical structure of the episodically enhanced intrusion flow in the channel in EXP1. During the peak of the first intrusion episode on day 20, the inflow velocity has a near-bottom maximum with a magnitude exceeding 20 cm $s^{-1}$ on the eastern slope of the channel at the depth of 150 m (Fig. 12h). Such bottom intensification does not exist in the Base run (Fig. 12c). Along with the bottom intensified inflow velocity is clear intrusion of slope water (the red patch in Fig. 12e). Isopycnals at the depth range of 100–200 m in the central part of the channel in EXP1 have a gentle upward tilt toward the eastern side of the channel (Fig. 12f), and they bend down close to the bottom of the eastern channel slope, consistent

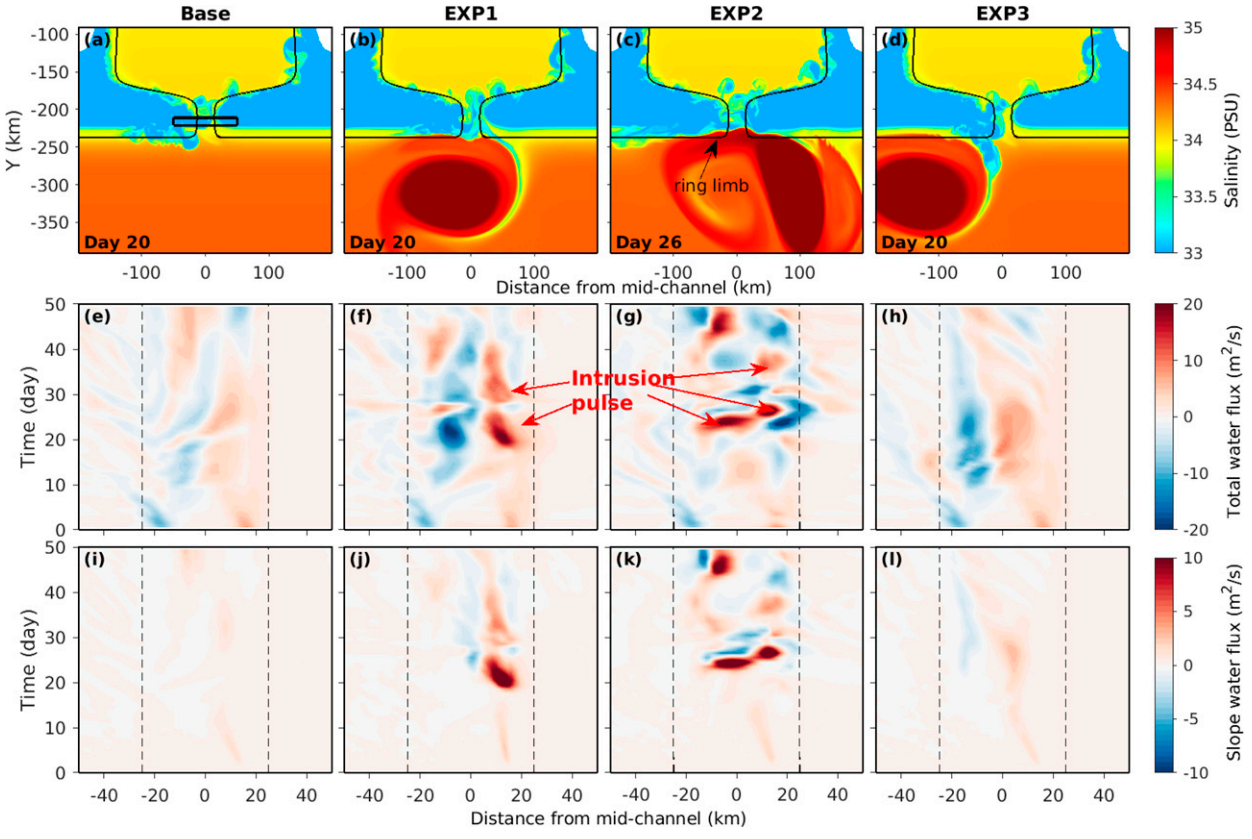


FIG. 9. (a)–(d) Surface salinity on selected days, (e)–(h) vertically integrated total volume flux, and (i)–(l) vertically integrated slope water passive tracer flux from four ROMS simulations. The thick black rectangle across the channel in (a) indicates the along-shelf range shown in lower panels.

with the bottom boundary layer dynamics. Meanwhile, the surface elevation has a dip in the middle of the channel, and the raising of the sea level toward the east over the eastern slope of the channel is consistent with the inflow there (Fig. 12g).

Bottom intensification of the along-channel velocity in EXP1 resembles the along-isobath velocity pattern of baroclinic CTWs over a sloping bottom (e.g., Wang and Mooers 1976; Huthnance 1986; Brink 1991). CTW, a type of subinertial topographic

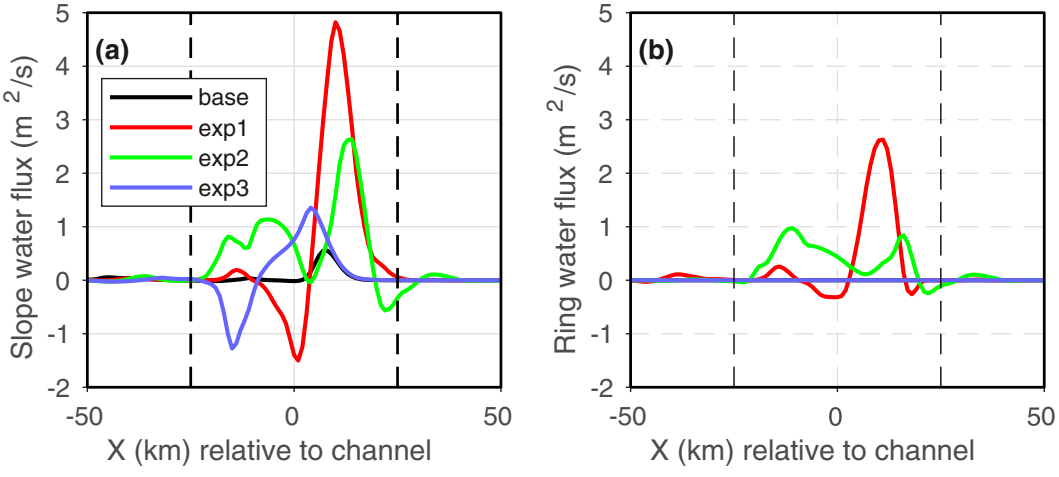


FIG. 10. Cross-channel distribution of vertically integrated, temporally averaged (days 20–40) along-channel fluxes of (a) slope and (b) ring waters from different numerical simulations (shown with different color). The flux is averaged over 10 km in the along-channel direction in the middle section of the channel. The dashed lines indicate edges of the channel.

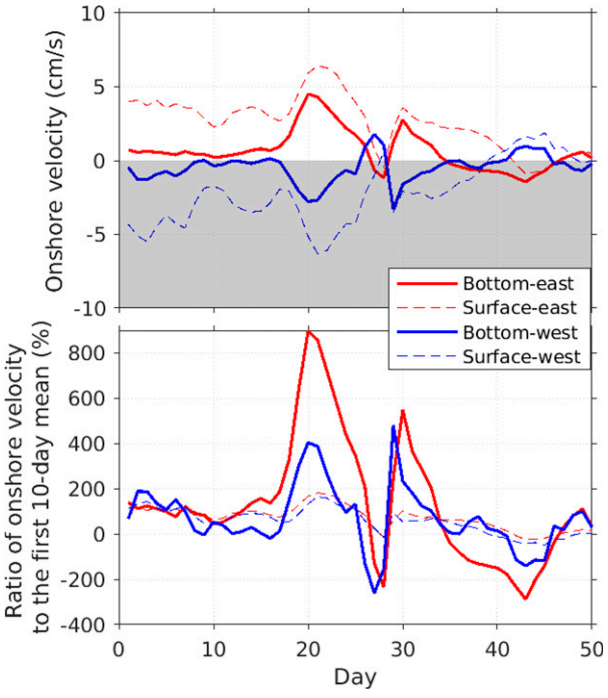


FIG. 11. Time series of (a) modeled along-channel velocity averaged over each of the four quadrants of the channel cross section and (b) the velocity normalized by the corresponding mean in the first 10 days. Results here are from ROMS simulation EXP1.

vorticity wave, can be generated by transient flows interacting with irregular seafloor topography, such as canyons (e.g., Kämpf 2012; Zhang and Lentz 2017). Irregular topography of the NEC can presumably interact with strong transient flows at the shelf edge induced by the impinging WCR and, through perturbing the isopycnals, generate baroclinic CTWs. Because CTWs in the north hemisphere propagate with the coast on the right, some of the waves generated at the mouth of the NEC would be able to (i) propagate along the eastern slope of the channel, (ii) take a right turn at the interior end of the channel, and then (iii) continue to propagate along the isobath into the GoM. It is likely that the pulse-like slope water intrusion in the NEC reflects oscillation and propagation of CTWs.

In order for baroclinic CTWs to propagate into the GoM, NEC has to be dynamically wide enough to allow the waves to propagate through. Cross-isobath length scale of baroclinic CTWs is related to both the cross-slope length and the baroclinic Rossby radius, $\delta_R = H_0 N/f$. Here, $H_0$ is a depth scale, and $N$ the buoyance frequency. In the NEC, because $H_0 \approx 200$ m, $N \approx 0.005\ \mathrm{s}^{-1}$, and $f \approx 10^{-4}\ \mathrm{s}^{-1}$, $\delta_R \approx 10$ km, much smaller than the 50-km width of the NEC. Meanwhile, by definition, the channel is wider than the side slope of the channel. Therefore, at least some baroclinic CTWs formed on the shelf edge can propagate into the NEC.

Along-isobath distribution of the velocity in EXP1 is consistent with CTW propagation. To demonstrate this, we extract near-bottom (20 m above the bottom) velocity along a section of the bended 200-m isobath starting at the southeastern corner of the channel and extending into the gulf (the bended black line in Fig. 2a). The velocity at every point on the 200-m isobath section is rotated to the local along-isobath direction. Hovmöller diagram of the along-isobath velocity shows two bands of enhanced positive values (as highlighted by the thick lines in Fig. 13a), starting in the channel on days 18 and 29, respectively, and a more diffused band of negative values in between. The bands of enhanced near-bottom velocity propagate along the isobath in a speed of ~0.25 m $\mathrm{s}^{-1}$, reaching 150 km in 7 days. Snapshots of the along-isobath velocity on selected cross-isobath sections (S1–S4, 24 km apart; see Fig. 2a for their location) show the velocity pattern and its evolution at each location (Fig. 14). It confirms bottom intensification of the along-isobath velocity at the 100–200-m isobath on each of the cross-isobath sections when the first band of positive near-bottom along-isobath velocity arrives.

Characteristics of the episodically bottom-intensified along-isobath flow in the NEC captured by both observations and the ROMS model agree with the mode-2 solution of the linear CTW model. If the 10-day time interval between ROMS-modeled and observed intrusion flow episodes is the CTW period $T_c$, and the 0.25 m $\mathrm{s}^{-1}$ along-isobath propagation speed of the intrusion signal is the CTW phase speed $c$, the along-shelf wavelength of the wave is $\lambda_c = cT_c \approx 220$ km. Here, the linear CTW model (Brink 1990, 2006) with constant $N \approx 0.005\ \mathrm{s}^{-1}$ and $f \approx 10^{-4}\ \mathrm{s}^{-1}$ is used to obtain the dispersion relation and mode shape of linear baroclinic CTWs propagating on the eastern slope of the channel in the ROMS model. The CTW model gives a mode-2 solution with wavenumber, frequency, mode shape resembling those observed and ROMS modeled (Fig. 15). In particular, the along-shelf velocity has a bottom intensification, qualitatively similar to that at the 100–200-m isobath in observations and the ROMS model. The CTW solution has a weak bottom-intensified along-shelf *return* (negative) flow at a greater depth, also qualitatively similar to the ROMS solution in Fig. 14. Moreover, the mode-2 dispersion curve of the linear CTW aligns with temporal and along-isobath scales of the episodically bottom-intensified along-isobath flow in observations and ROMS solutions (Fig. 15d). All these confirm that the observed episodic enhancement of slope water intrusion in the NEC is caused by CTWs.

Note that there are also other perturbation signals propagating along-isobath in lower speeds in the ROMS solution (dashed lines in Fig. 13a), likely representing CTWs of higher modes with slower phase propagation. In particular, the blue dashed line in Fig. 13a likely represent mode-4 CTW because the propagation speed of the associated signal, ~0.08 m $\mathrm{s}^{-1}$, matches phase speed of the mode-4 CTW resolved by the linear CTW model (green line in Fig. 15d).

The mode-2 CTW with a period of ~10 days appears to dominate the flow response in the channel, which is intriguing. Even though the underlying mechanism is unclear, we here provide some speculation on the dynamics to motivate future studies. The mode-2 CTW resolved by the linear CTW model shows a bottom-intensified structure on the sloping part of the idealized topography (Figs. 15a–c). This slope-focused structure is not sensitive to the extent of the domain on the onshore and offshore ends where the bottom is flat. This

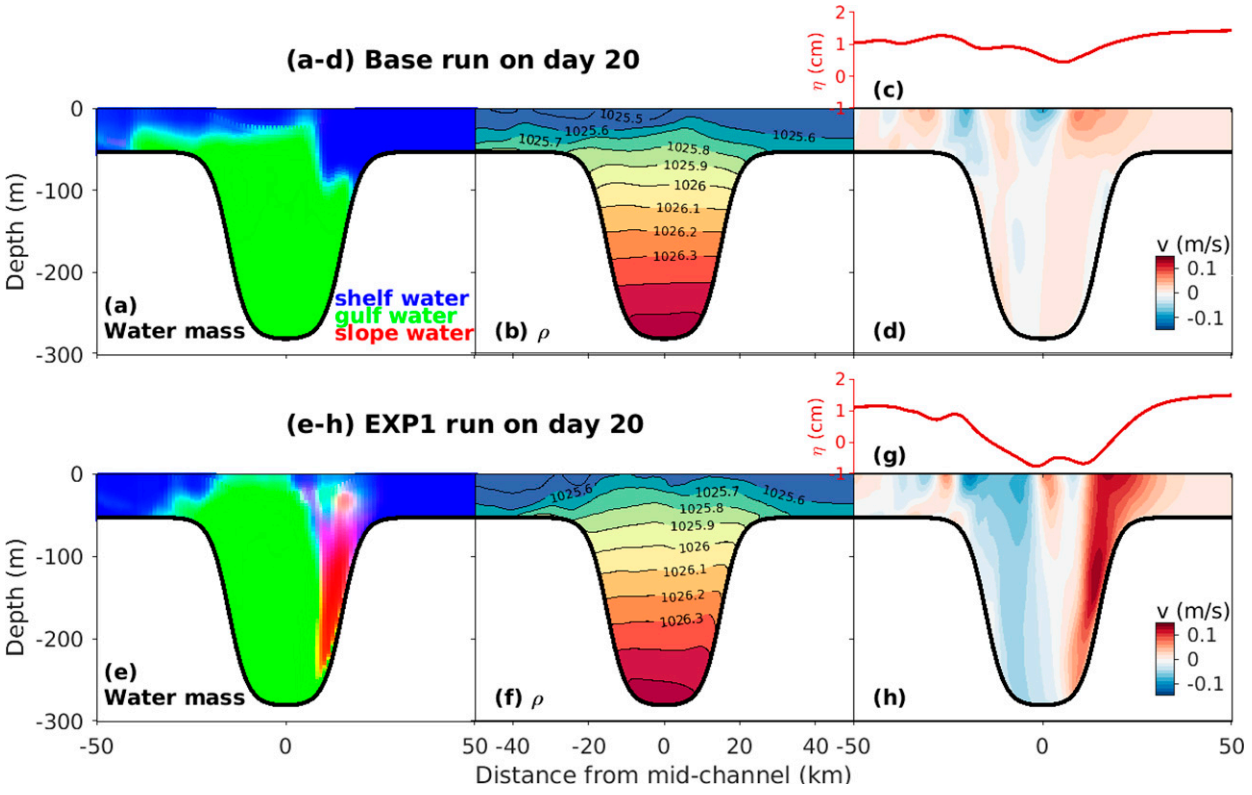


FIG. 12. Water mass, potential density, surface elevation, and along-channel velocity on day 20 in (top) the Base run and (bottom) EXP1.

suggests that the mode-2 CTW is really a slope mode of the topographic vorticity wave and associated with potential vorticity variation induced by the interaction between transient cross-isobath flow and the sloping bottom. The influence of the sloping bottom is the strongest near the bottom, which results in the bottom-intensified structure, i.e., bottom trapping. Meanwhile, stratification suppresses upward extent of the bottom influence and further intensifies the bottom trapping (Brink 2006). The required transient cross-isobath flow in the channel results presumably from impingement of the

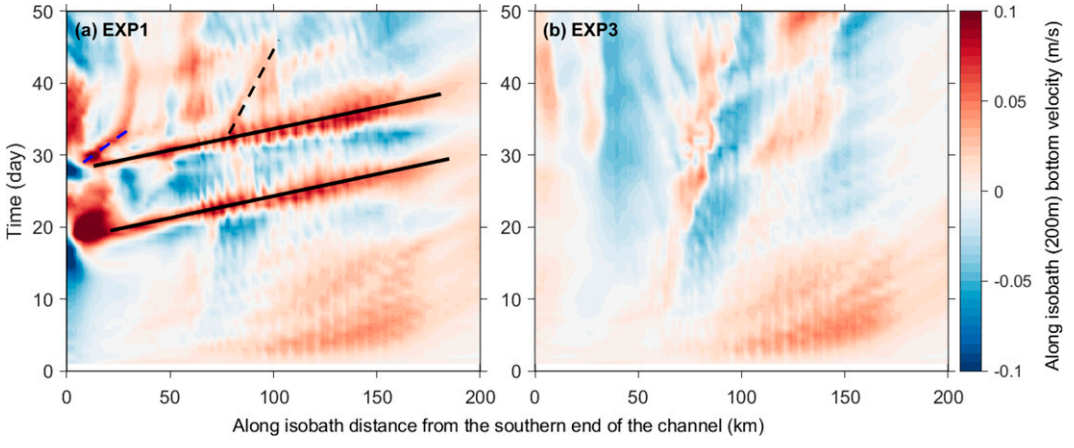


FIG. 13. Hovmöller diagram of along-isobath velocity at 20 m above the bottom along a section of the 200-m isobath (see Fig. 2a for its location) in (a) EXP1 and (b) EXP3. Positive velocity here denotes flow in the same direction as CTW phase propagation. The solid lines in (a) highlight two bands of high velocity indicating along-isobath downwave phase propagation of CTWs starting from the eastern slope of the channel into the gulf after the ring impinges onto the shelf; the blue and black dashed lines represent possible propagation signals of CTWs of higher modes. Note the along-isobath oscillation of the signal is caused by interpolation of the velocity on the horizontally staggered ROMS grid.

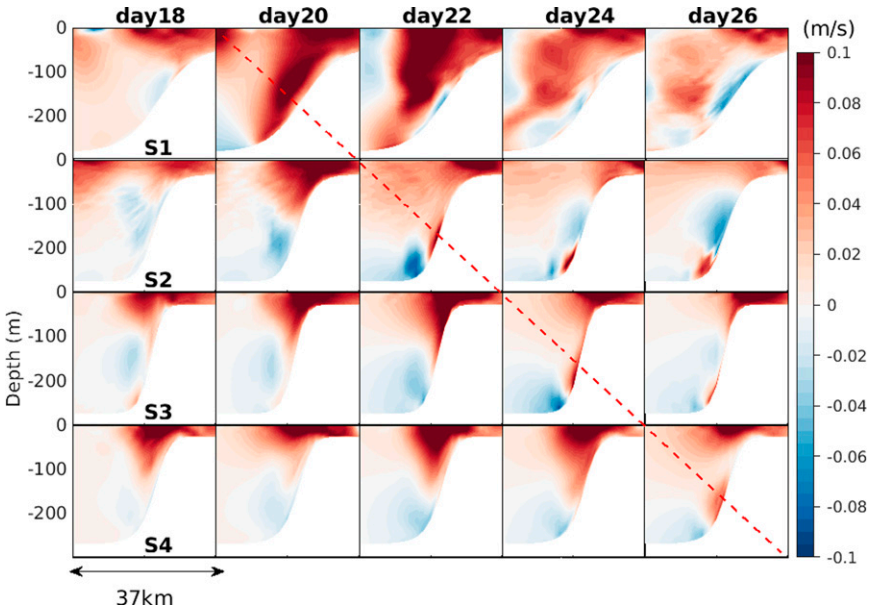


FIG. 14. Snapshots of along-isobath velocity distribution on four selected cross-isobath sections (see Fig. 2a for their locations) on different days in EXP1. The red dashed line roughly indicates the arrival of the positive near-bottom along-isobath velocity in the first band (the lower solid line in Fig. 13) at each of the sections.

ring. It is likely that the particular mode-2 CTW of the 10-day period dominates because ring-induced transient cross-isobath flows excite it more efficiently than other mode-2 CTWs and CTWs of other modes. Another possibility is that CTWs of other modes propagate away without inducing net intrusion of the offshore water. For instance, the mode-1 CTW resolved by the linear CTW model has a nearly barotropic structure covering the entire shelf (not shown) and a phase speed of ~2.5 m $s^{-1}$ (Fig. 15d). If generated, the mode-1 wave likely propagates away rapidly as a linear wave and results in no net along-channel intrusion of the offshore water.

The mode-2 CTWs excited by the interaction between impinging WCRs and the NEC are likely nonlinear. Oscillatory flows of a linear long wave would not drive net along-isobath transport. To drive the net intrusion of offshore water, CTWs propagating through the NEC have to be nonlinear with some degree of skewness. Nonlinearity of the mode-2 CTW could result from interaction of the CTW with flows or other waves. The former is consistent with the fact that phase speed of the mode-2 CTW, ~0.25 m $s^{-1}$, is similar to the inflow velocity on the northern slope of the channel (Fig. 12h). A number of other potential factors could also cause nonlinearity of the waves, including instability of impinging WCRs and complex topography of the NEC. As shown by the SST images and ROMS simulations, instabilities are ubiquitous on the ring periphery. When a distorted ring with outward extending limbs (or other submesoscale features) impinges onto the shelf edge, local responses at the shelf edge are presumably transient, and CTWs of different wavenumbers (and frequencies) are likely excited. Meanwhile, bending of the isobath at the gulf end of the NEC could scatter CTWs and form waves of other modes (Wilkin and Chapman 1990). Nonlinear interaction of CTWs of different wavenumber, frequencies, or modes could then cause skewness in the along-isobath flow and result in net inflow in the NEC during the ring impingement. The dynamics of these nonlinear processes is beyond the scope of this study and left for future studies.

EXP2 shows qualitatively similar patterns of along-isobath propagation of velocity perturbation and stronger bottom intensification of the along-isobath velocity (Fig. 16). These are all consistent with the greatly enhanced subsurface intrusion of slope and ring waters in the channel in EXP2. Meanwhile, EXP3 shows a much slower (~0.02 m $s^{-1}$) along-isobath propagation of weak velocity perturbation (Fig. 13b) with no significantly enhanced near-bottom flow on the cross-isobath sections (not shown), which is consistent with a lack of clear enhancement of the intrusion flow in the channel in EXP3 (Fig. 10). Note that the ring in EXP3 impinges onto the shelf edge to the far west of the channel. Close examination of the model result shows that flow disturbances induced by the ring impingement propagate westward (downwave) farther away from the channel, as demonstrated in the literature (e.g., Cherian and Brink 2018; ZG15A). The slow along-isobath propagation of the weak perturbation in the gulf results from flow instabilities in the channel associated with the streamer forming to the east of the ring (Fig. 9d). Therefore, the impingement in EXP3 does not produce major perturbation in the channel. These differences in the simulations suggest that ring impingement location on the shelf edge is a key factor determining whether baroclinic CTWs excited by ring–topography interaction can propagate into the NEC and induce strong intrusion of offshore water into the GoM.

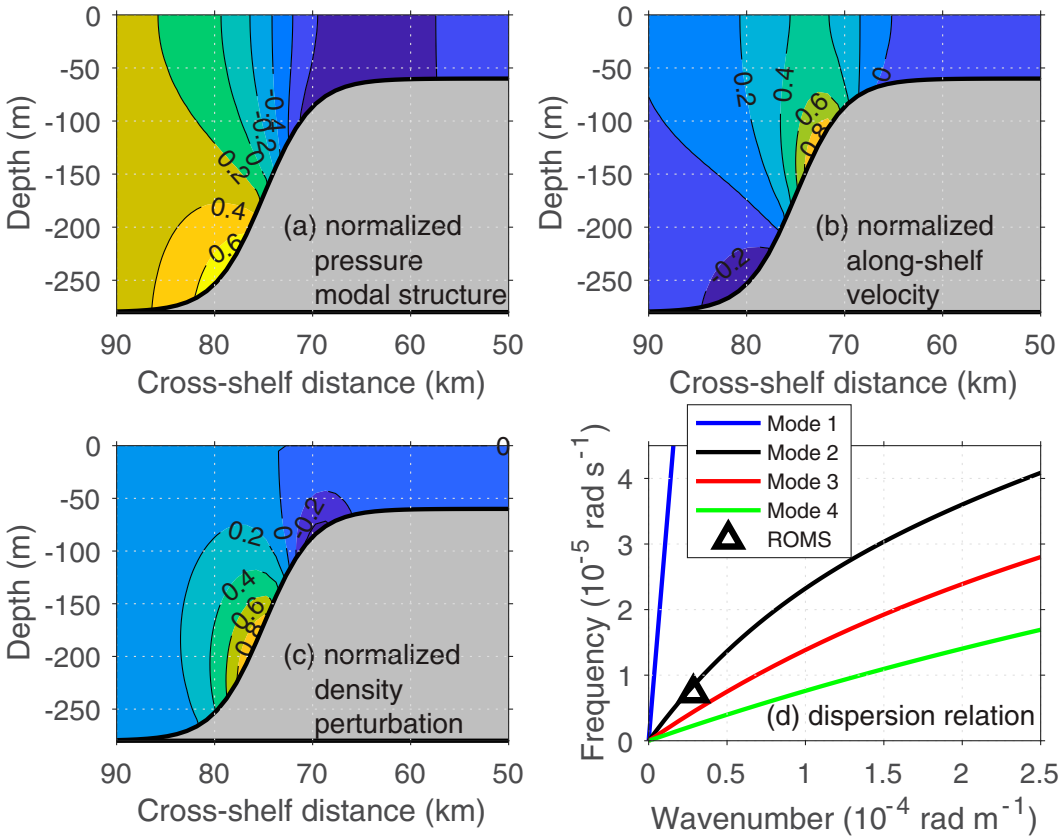


FIG. 15. Cross-shelf section of the modal structure of normalized (a) pressure, (b) along-shelf velocity, and (c) density perturbation, as well as (d) the corresponding dispersion relation (black line) of a mode-2 wave solution given by the linear CTW model. The values in (a)–(c) are normalized by the corresponding maximum values. The black triangle in (d) indicates the wavenumber and frequency corresponding to the ROMS-modeled episodic bottom-intensification of the along-isobath flow in the channel; the blue, red, and green lines in (d) are the dispersion relation of the mode-1, mode-3, and mode-4 CTWs given by the linear CTW model.

### b. *WCR impact on the GoM*

Despite the episodic nature, WCR-induced enhancement of offshore water intrusion may contribute substantially to the overall offshore water intrusion into the GoM. Here, we seek to provide a back-of-the-envelope estimate of the contribution. WCR's influence on the offshore water intrusion changes with the ring impinging location on the shelf edge with pronounced enhancement occurring when a ring impinges onto the shelf edge northeast (upwave) of or near the NEC. The ring impact is weak when a ring impinges onto the far downwave of the NEC (e.g., the south edge of the Georges Bank). Our analysis of the SSH data shows that, on average, ~6% of the time there is a ring within 50 km of the shelf edge to the upwave (northeast) of the NEC (Fig. 4b). This ring occupancy in the slope sea region varies greatly from year to year. In 1993, 1994, 2010, and 2017, the *upwave* ring-occupying time is ~20% (Fig. 4b). The ring-induced *enhancement* of slope/ring water intrusion in the channel averaged over days 20–40 is $53 \times 10^3$ m$^3$ s$^{-1}$ in both EXP1 and EXP2, which is 27% of the mean slope water flux (~$200 \times 10^3$ m$^3$ s$^{-1}$) measured at the NEC in 1976–80 (Smith 1983; Ramp et al. 1985). Assuming this ring-induced enhancement applies to all WCRs impinging onto the shelf edge upwave of the NEC, WCRs in 1993, 1994, 2010, and 2017 would directly contribute to 5.4% of the annual slope water flux into the GoM. Note that this weak contribution is a conservative estimate as we neglect WCRs impinging onto the shelf edge slightly downwave (west) of the NEC, which, as demonstrated by R16, could also induce substantial enhancement of the offshore water intrusion.

Besides the direct enhancement of the slope water intrusion, WCR could also affect conditions in the GoM *indirectly* through other pathways, such as modifying the ambient slope water or the upstream shelf water. First, mixing of the high-temperature, high-salinity ring water with the surrounding water in the slope sea could modify properties of the source slope water that intrudes into the GoM. This indirect pathway is consistent with an apparent correspondence between the interannual variabilities of WCR activities and surface temperature in the slope sea: in all years with ring-occupying time $d_{\text{ring}} > 200$ days (i.e., 1993, 1994, 1995, 1999, 2014, 2015, 2016; Fig. 4b), SST is abnormally high in the slope sea (see Fig. 2b in Chen et al. 2020); moreover, the relatively high occupancy

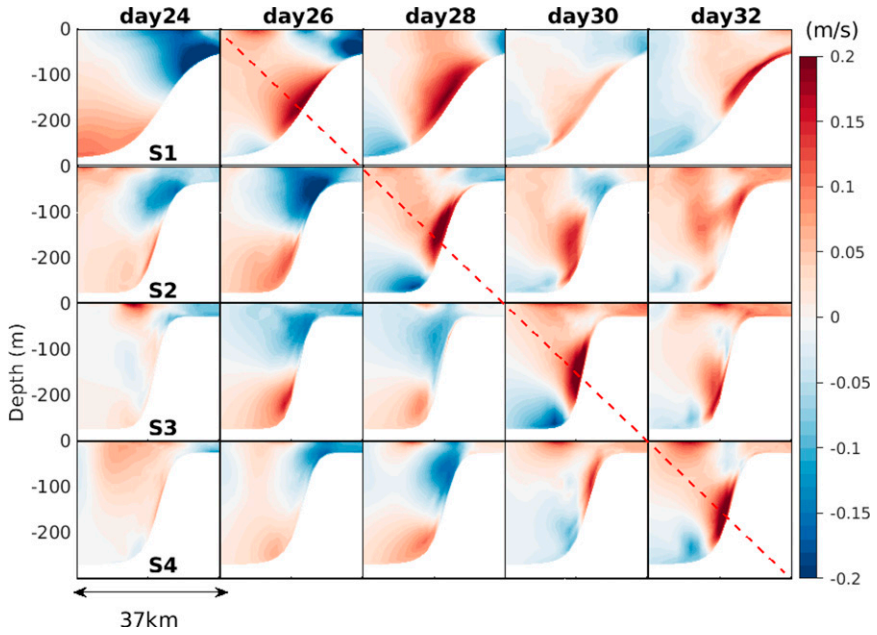


FIG. 16. As in Fig. 14, but for ROMS simulation EXP2.

of WCRs in the slope sea in 2014–16 is consistent with the slope water near the GoM being the warmest over the 37 years period of 1982–2018 (Chen et al. 2020). These suggest that the indirect WCR influence through modifying the source slope water is at least a contributor. Note that this indirect effect does not require WCRs to impinge onto the shelf edge. Second, impinging WCRs could break the shelf-slope barrier and directly push ring/slope water onto a shelf (ZG15A). WCRs impinging onto the Scotian shelf could modify properties of the upstream water that flows into the GoM on the shelf (Brickman et al. 2018). Both of these pathways likely increase heat and salt flux into the gulf. Meanwhile, WCRs impinging onto the Scotian shelf could also induce long CTWs that propagate southwestward along the shelf edge. These long CTWs could then modify the transport in the NEC. How this second type of indirect influence of the WCRs impinging onto the far upwave shelf remains unclear. With the increasingly unstable Gulf Stream (Andres 2016) and more WCRs being shed from the Gulf Stream into the slope sea in the northwest Atlantic, all these indirect influences of the WCRs, together with the ring-induced direct intrusion in the NEC, will likely result in stronger influence of the open ocean processes in the GoM.

## 5. Summary

This study combines in situ mooring data, satellite SST and SSH data, and idealized numerical simulations to examine how the intrusion flow of slope water into GoM through the NEC is directly impacted by Gulf Stream WCRs. While our dynamical analysis focuses on episodic events, statistics of the WCRs on seasonal to interannual time scales are also presented. The following are key findings from the analysis:

1) The slope sea region offshore of the GoM has the highest WCR occupancy in the entire slope sea in the Northwest Atlantic and is thus a hotspot of WCR activities. The NEC is within 50-km proximity of a WCR for over 50% of the time in the last 26 years. There is thus a great potential of WCRs impinging onto the shelf edge near the NEC and influencing the conditions in the GoM.
2) Ring activities in the slope sea off the GoM are highly variable. Interannual variability of the ring activities in the region is significantly correlated with variability of bottom-layer salinity at the NEC, suggesting that more ring activities near the GoM lead to either stronger intrusion of the high-salinity slope water (a *direct* pathway) or intrusion of higher-salinity slope water into the NEC (an *indirect* pathway).
3) Intrusion of slope water into the NEC is directly impacted by WCRs impinging onto the nearby shelf edge, and the impact varies with the impingement location relative to the NEC. Mooring data show pulse-like slope water intrusion in the NEC when a WCR impinges on the shelf edge near or upwave to the NEC, while limited impact is observed when a WCR impinges onto the shelf edge to the far west of the NEC.
4) The pulse-like intrusion of slope water coincided with a bottom-intensified along-channel flow, prompting the hypothesis of baroclinic CTWs as the underlying mechanism of the episodically enhanced intrusion. Idealized ROMS simulations and a linear CTW model together confirm that CTWs induced by impingement of WCRs on the shelf edge propagate into the GoM through the NEC and then enhance the intrusion of slope and ring waters into the gulf. This finding emphasizes the importance of irregular shelf edge topography in inducing cross-shelf exchange.

Combining the statistical ring analysis and modeled enhancement of the ring-induced offshore water intrusion, we estimate that in years of high ring activities in the slope sea region off the GoM, ring-induced enhancement of the slope water intrusion in the NEC could account for at least 5.4% of the annual total slope water intrusion into the GoM. However, influence of WCRs on conditions in the GoM can be higher as WCRs may also affect conditions of the source slope and shelf waters and perturb the flow in the NEC through long CTWs. To quantify the overall influence of WCRs on the GoM requires a thorough study of all these influencing pathways.

*Acknowledgments.* This study is supported by the National Science Foundation through Grant OCE-1634965.

*Data availability statement.* The mooring data at the Northeast Channel were downloaded from the publicly accessible data server (http://www.neracoos.org/thredds/UMO_SOS_historical_realtime_agg.html) maintained by Northeastern Regional Association of Coastal Ocean Observing Systems. Gridded satellite altimetry data were download from the public server of European Union Copernicus Marine Environmental Monitoring Service (https://cds.cli-mate.copernicus.eu/cdsapp#!/dataset/satellite-sea-level-global?tab=overview). Satellite data of sea surface temperature were downloaded from the publicly accessible server at https://coastwatch.pfeg.noaa.gov/erddap/griddap/jplG1SST.html. Satellite chlorophyll data are from NESDIS Center for Satellite Applications and Research at NOAA (http://www.star.nesdis.noaa.gov/socd/mecb/color).

## REFERENCES

Allen, J. S., 1980: Models of wind-driven currents on the continental shelf. *Annu. Rev. Fluid Mech.*, **12**, 389–433, https://doi.org/10.1146/annurev.fl.12.010180.002133.

Andres, M., 2016: On the recent destabilization of the Gulf Stream path downstream of Cape Hatteras: Gulf Stream Path Destabilization. *Geophys. Res. Lett.*, **43**, 9836–9842, https://doi.org/10.1002/2016GL069966.

Bigelow, H. B., 1927: Physical oceanography of the Gulf of Maine. *Bull. U.S. Bur. Fish.*, **40**, 511–1027.

Bisagni, J. J., O. C. Nichols, and R. Pettipas, 2019: Interannual variability of Gulf Stream warm-core ring interactions with the outer continental shelf and potential broad scale relationships with longfin squid (*Doryteuthis pealeii*) relative abundance, 1981–2004. *ICES J. Mar. Sci.*, **76**, 1257–1270, https://doi.org/10.1093/icesjms/fsz144.

Brickman, D., D. Hebert, and Z. Wang, 2018: Mechanism for the recent ocean warming events on the Scotian Shelf of eastern Canada. *Cont. Shelf Res.*, **156**, 11–22, https://doi.org/10.1016/j.csr.2018.01.001.

Brink, K. H., 1990: On the damping of free coastal-trapped waves. *J. Phys. Oceanogr.*, **20**, 1219–1225, https://doi.org/10.1175/1520-0485(1990)020<1219:OTDOFC>2.0.CO;2.

——, 1991: Coastal-trapped waves and wind-driven currents over the continental shelf. *Annu. Rev. Fluid Mech.*, **23**, 389–412, https://doi.org/10.1146/annurev.fl.23.010191.002133.

——, 2006: Coastal-trapped waves with finite bottom friction. *Dyn. Atmos. Oceans*, **41**, 172–190, https://doi.org/10.1016/j.dynatmoce.2006.05.001.

Brooks, D. A., 1987: The influence of warm-core rings on slope water entering the Gulf of Maine. *J. Geophys. Res.*, **92**, 8183–8196, https://doi.org/10.1029/JC092iC08p08183.

Chaudhuri, A. H., A. Gangopadhyay, and J. J. Bisagni, 2009: Interannual variability of Gulf Stream warm-core rings in response to the North Atlantic Oscillation. *Cont. Shelf Res.*, **29**, 856–869, https://doi.org/10.1016/j.csr.2009.01.008.

Chelton, D. B., M. G. Schlax, R. M. Samelson, and R. A. de Szoeke, 2007: Global observations of large oceanic eddies. *Geophys. Res. Lett.*, **34**, L15606, https://doi.org/10.1029/2007GL030812.

Chen, K., R. He, B. S. Powell, G. G. Gawarkiewicz, A. M. Moore, and H. G. Arango, 2014: Data assimilative modeling investigation of Gulf Stream Warm Core Ring interaction with continental shelf and slope circulation. *J. Geophys. Res. Oceans*, **119**, 5968–5991, https://doi.org/10.1002/2014JC009898.

Chen, Z., Y. Kwon, K. Chen, P. Fratantoni, G. Gawarkiewicz, and T. M. Joyce, 2020: Long-term SST variability on the northwest Atlantic continental shelf and slope. *Geophys. Res. Lett.*, **47**, e2019GL085455, https://doi.org/10.1029/2019GL085455.

Cherian, D. A., and K. H. Brink, 2016: Offshore transport of shelf water by deep-ocean eddies. *J. Phys. Oceanogr.*, **46**, 3599–3621, https://doi.org/10.1175/JPO-D-16-0085.1.

——, and ——, 2018: Shelf flows forced by deep-ocean anticyclonic eddies at the shelf break. *J. Phys. Oceanogr.*, **48**, 1117–1138, https://doi.org/10.1175/JPO-D-17-0237.1.

Churchill, J. H., P. C. Cornillon, and G. W. Milkowski, 1986: A cyclonic eddy and shelf-slope water exchange associated with a Gulf Stream warm-core ring. *J. Geophys. Res.*, **91**, 9615–9623, https://doi.org/10.1029/JC091iC08p09615.

Clarke, A. J., 1977: Observational and numerical evidence for wind-forced coastal trapped long waves. *J. Phys. Oceanogr.*, **7**, 231–247, https://doi.org/10.1175/1520-0485(1977)007<0231:OANEFW>2.0.CO;2.

Du, J., W. G. Zhang, and Y. Li, 2021: Variability of deep water in Jordan Basin of the Gulf of Maine: Influence of Gulf Stream warm core rings and the Nova Scotia Current. *J. Geophys. Res. Oceans*, **126**, https://doi.org/10.1029/2020JC017136.

Early, J. J., R. M. Samelson, and D. B. Chelton, 2011: The evolution and propagation of quasigeostrophic ocean eddies. *J. Phys. Oceanogr.*, **41**, 1535–1555, https://doi.org/10.1175/2011JPO4601.1.

Fratantoni, P. S., and R. S. Pickart, 2007: The Western North Atlantic shelfbreak current system in summer. *J. Phys. Oceanogr.*, **37**, 2509–2533, https://doi.org/10.1175/JPO3123.1.

Gangopadhyay, A., G. Gawarkiewicz, E. N. S. Silva, M. Monim, and J. Clark, 2019: An observed regime shift in the formation of warm core rings from the Gulf Stream. *Sci. Rep.*, **9**, 12319, https://doi.org/10.1038/s41598-019-48661-9.

Garfield, N., and D. L. Evans, 1987: Shelf water entrainment by Gulf Stream warm-core rings. *J. Geophys. Res.*, **92**, 13 003–13 012, https://doi.org/10.1029/JC092iC12p13003.

Houghton, R. W., and R. G. Fairbanks, 2001: Water sources for Georges Bank. *Deep-Sea Res. II*, **48**, 95–114, https://doi.org/10.1016/S0967-0645(00)00082-5.

Huthnance, J., 1986: The Rockall slope current and shelf-edge processes. *Proc. Roy. Soc. Edinburgh*, **88B**, 83–101, https://doi.org/10.1017/S0269727000004486.

Huthnance, J. M., 1978: On coastal trapped waves: Analysis and numerical calculation by inverse iteration. *J. Phys. Oceanogr.*,

**8**, 74–92, https://doi.org/10.1175/1520-0485(1978)008<0074:OCTWAA>2.0.CO;2.

Isern-Fontanet, J., E. García-Ladona, and J. Font, 2003: Identification of marine eddies from altimetric maps. *J. Atmos. Oceanic Technol.*, **20**, 772–778, https://doi.org/10.1175/1520-0426(2003)20<772:IOMEFA>2.0.CO;2.

Joyce, T., and Coauthors, 1984: Rapid evolution of a Gulf Stream warm-core ring. *Nature*, **308**, 837–840, https://doi.org/10.1038/308837a0.

Joyce, T. M., J. K. B. Bishop, and O. B. Brown, 1992: Observations of offshore shelf-water transport induced by a warm-core ring. *Deep-Sea Res.*, **39**, S97–S113, https://doi.org/10.1016/S0198-0149(11)80007-5.

Kämpf, J., 2012: Lee effects of localized upwelling in a shelf-break canyon. *Cont. Shelf Res.*, **42**, 78–88, https://doi.org/10.1016/j.csr.2012.05.005.

Knox, J. A., and P. R. Ohmann, 2006: Iterative solutions of the gradient wind equation. *Comput. Geosci.*, **32**, 656–662, https://doi.org/10.1016/j.cageo.2005.09.009.

Malan, N., B. Backeberg, A. Biastoch, J. V. Durgadoo, A. Samuelsen, C. Reason, and J. Hermes, 2018: Agulhas Current meanders facilitate shelf-slope exchange on the East Agulhas Bank. *J. Geophys. Res. Oceans*, **123**, 4762–4778, https://doi.org/10.1029/2017JC013602.

——, and Coauthors, 2020: Eddy-driven cross-shelf transport in the East Australian current separation zone. *J. Geophys. Res. Oceans*, **125**, e2019JC015613, https://doi.org/10.1029/2019JC015613.

Mertz, F., and J. F. Legeais, 2020: Product user guide and specification: Sea level v1.2. ECMWF Copernicus Rep., 30 pp., https://datastore.copernicus-climate.eu/documents/satellite-sea-level/D3.SL.1-v1.2_PUGS_of_v1DT2018_SeaLevel_products_v2.4.pdf.

Penven, P., I. Halo, S. Pous, and L. Marié, 2014: Cyclogeostrophic balance in the Mozambique Channel. *J. Geophys. Res. Oceans*, **119**, 1054–1067, https://doi.org/10.1002/2013JC009528.

Pershing, A. J., and Coauthors, 2015: Slow adaptation in the face of rapid warming leads to collapse of the Gulf of Maine cod fishery. *Science*, **350**, 809–812, https://doi.org/10.1126/science.aac9819.

Pettigrew, N. R., C. P. Fikes, and M. K. Beard, 2011: Advances in the ocean observing system in the Gulf of Maine: Technical capabilities and scientific results. *Mar. Technol. Soc. J.*, **45**, 85–97, https://doi.org/10.4031/MTSJ.45.1.11.

Ramp, S. R., R. J. Schlitz, and W. R. Wright, 1985: The deep flow through the Northeast Channel, Gulf of Maine. *J. Phys. Oceanogr.*, **15**, 1790–1808, https://doi.org/10.1175/1520-0485(1985)015<1790:TDFTTN>2.0.CO;2.

Ryan, J. P., J. A. Yoder, and D. W. Townsend, 2001: Influence of a Gulf Stream warm-core ring on water mass and chlorophyll distributions along the southern flank of Georges Bank. *Deep-Sea Res. II*, **48**, 159–178, https://doi.org/10.1016/S0967-0645(00)00117-X.

Schlitz, R. J., and E. B. Cohen, 1984: A nitrogen budget for the Gulf of Maine and Georges Bank. *Biol. Oceanogr.*, **3**, 203–222.

Shchepetkin, A. F., and J. C. McWilliams, 2005: The Regional Oceanic Modeling System (ROMS): A split-explicit, free-surface, topography-following-coordinate oceanic model. *Ocean Modell.*, **9**, 347–404, https://doi.org/10.1016/j.ocemod.2004.08.002.

Smith, P. C., 1983: The mean and seasonal circulation off southwest Nova Scotia. *J. Phys. Oceanogr.*, **13**, 1034–1054, https://doi.org/10.1175/1520-0485(1983)013<1034:TMASCO>2.0.CO;2.

——, R. W. Houghton, R. G. Fairbanks, and D. G. Mountain, 2001: Interannual variability of boundary fluxes and water mass properties in the Gulf of Maine and on Georges Bank: 1993–1997. *Deep-Sea Res. II*, **48**, 37–70, https://doi.org/10.1016/S0967-0645(00)00081-3.

——, N. R. Pettigrew, P. Yeats, D. W. Townsend, and G. Han, 2012: Regime shift in the Gulf of Maine. *Amer. Fish. Soc. Symp.*, **79**, 185–203.

Townsend, D. W., 1998: Sources and cycling of nitrogen in the Gulf of Maine. *J. Mar. Syst.*, **16**, 283–295, https://doi.org/10.1016/S0924-7963(97)00024-9.

——, N. D. Rebuck, M. A. Thomas, L. Karp-Boss, and R. M. Gettings, 2010: A changing nutrient regime in the Gulf of Maine. *Cont. Shelf Res.*, **30**, 820–832, https://doi.org/10.1016/j.csr.2010.01.019.

Wang, D.-P., and C. N. K. Mooers, 1976: Coastal-trapped waves in a continuously stratified ocean. *J. Phys. Oceanogr.*, **6**, 853–863, https://doi.org/10.1175/1520-0485(1976)006<0853:CTWIAC>2.0.CO;2.

Warner, J. C., C. R. Sherwood, H. G. Arango, and R. P. Signell, 2005: Performance of four turbulence closure models implemented using a generic length scale method. *Ocean Modell.*, **8**, 81–113, https://doi.org/10.1016/j.ocemod.2003.12.003.

Wilkin, J. L., and D. C. Chapman, 1990: Scattering of coastal-trapped waves by irregularities in coastlines and topography. *J. Phys. Oceanogr.*, **20**, 396–421, https://doi.org/10.1175/1520-0485(1990)020<0396:SOCTWB>2.0.CO;2.

Wright, D. G., D. A. Greenberg, J. W. Loder, and P. C. Smith, 1986: The steady-state barotropic response of the Gulf of Maine and adjacent regions to surface wind stress. *J. Phys. Oceanogr.*, **16**, 947–966, https://doi.org/10.1175/1520-0485(1986)016<0947:TSSBRO>2.0.CO;2.

Xue, H., F. Chai, and N. R. Pettigrew, 2000: A model study of the seasonal circulation in the Gulf of Maine. *J. Phys. Oceanogr.*, **30**, 25, https://doi.org/10.1175/1520-0485(2000)030<1111:AMSOTS>2.0.CO;2.

Zhang, W. G., and G. G. Gawarkiewicz, 2015a: Dynamics of the direct intrusion of Gulf Stream ring water onto the Mid-Atlantic Bight shelf. *Geophys. Res. Lett.*, **42**, 7687–7695, https://doi.org/10.1002/2015GL065530.

——, and ——, 2015b: Length-scale of the finite-amplitude meanders of shelfbreak fronts. *J. Phys. Oceanogr.*, **45**, 2598–2620, http://doi.org/10.1175JPO-D-14-0249.1.

——, and S. J. Lentz, 2017: Wind-driven circulation in a shelf valley. Part I: Mechanism of the asymmetrical response to along-shelf winds in opposite directions. *J. Phys. Oceanogr.*, **47**, 2927–2947, https://doi.org/10.1175/JPO-D-17-0083.1.

——, and J. Partida, 2018: Frontal subduction of the Mid-Atlantic Bight shelf water at the onshore edge of a warm-core ring. *J. Geophys. Res. Oceans*, **123**, 7795–7818, https://doi.org/10.1029/2018JC013794.